

Modeling topographic effects on transport of tracers in the bottom boundary layer using RANS-models

Philosophiae Doctor Thesis

Kristin Rygg

Geophysical Institute
University of Bergen
Norway

UniComputing



April, 2011

Preface

This dissertation is submitted as a partial fulfillment of the requirements for the degree Doctor of Philosophy (PhD) at the Geophysical Institute, University of Bergen. The project is funded by the European Project EU IP CarboOcean 511176-2 and The Research Council of Norway through NFR 146526/420: Cordino.

The project started in September 2007, and since then I have been employed at the Computational Mathematical Unit (CMU), at UniComputing, UniResearch. This has been my daily working place. My main supervisor has been Professor Peter Mosby Haugan from the Geophysical Institute and my co-supervisor has been Professor Guttorm Alendal from the Department of Mathematics.

The main focus of this thesis is the effect of topographic features on the transport of tracers in the bottom boundary layer. The thesis covers two specific studies; transport of CO₂ which is directly introduced into the deep ocean and transport of passive food particles to cold-water corals. The study is performed using Reynolds Averaged Navier Stokes Models (RANS) on a relative small scale with horizontal grid sizes ranging from 75 meter to approximately 1 meter.

A general background for the study is given in Part I, and Part II consists of the four included papers.

Papers included in this thesis

The following papers are included in this thesis;

Paper A: Dissolution of a CO₂ lake, modeled by using an advanced vertical turbulence mixing scheme, L.I. Enstad, K. Rygg, G. Alendal, and P. M. Haugan, International Journal of Greenhouse Gas Control, 2, 2008

Paper B: Simulating CO₂ transport into the ocean from a CO₂ lake at the seafloor using a z - and a σ -coordinate model, K. Rygg, L. I. Enstad and G. Alendal, Ocean Dynamics, Vol 59 (6), Special issue: The 14th International Biennial Conference of the Joint Numerical Sea Modeling Group (JONSMOD), 2009

Paper C: Flow over a backward-facing step, a numerical study comparing a z - and a σ -coordinate model, K. Rygg, G. Alendal, and P. M. Haugan, Under revision for publication in Ocean Dynamics, 2011

Paper D: Topographically controlled food transport to cold-water corals, K. Rygg, G. Alendal, and P. M. Haugan, Submitted to Continental Shelf Research, 2011

As all the papers are written in collaboration with other scientists, some clarifications regarding my contributions are necessary. Paper A explores the concept of a three dimensional CO₂ lake in the deep ocean using the general circulation model, the MITgcm, coupled with GOTM. Dr. Lars Inge Enstad did the programming and calculations related to this paper and also wrote the introduction and the methods section. My contribution was related to the literature review, and by writing the results and the discussion section. Professor Guttorm Alendal and Professor Peter M. Haugan contributed with comments and suggestions. In Paper B the study is extended to include topographic features, and is performed using both the MITgcm and the Bergen Ocean Model coupled with GOTM. The concept of the paper is a product of discussions between the authors. Both the programming part and the writing part were done by me. All authors contributed with discussions, comments, and suggestions. Some routines for coupling the MITgcm and GOTM developed for Paper A (written by Dr. Lars Inge Enstad) were also used in this paper. Paper C is a convergence study comparing two ocean models with different vertical coordinate system. Here the concepts were developed during discussions by all authors. In this paper I was responsible for both the calculations and the writing process. All authors contributed with suggestions and comments. Also for paper D, developing the concept was a joint project while the writing process and the simulation process were mainly my responsibility.

Acknowledgments

The process of working with this thesis has been instructive, inspiring, exciting, challenging, fun, but also at times long and winding. Many people have contributed, both scientifically and also socially.

First of all I would like to thank my two supervisors, Peter Mosby Haugan and Guttorm Alendal for good cooperation, helpful comments, interesting discussions, and the for the freedom you have given me to develop the project according to my own interests. I would also like to thank Jarle Berntsen for patiently supervising a former student, whenever I needed special BOM advice. I am also obliged to Lars Inge Enstad for all help in the beginning of my PhD, for MITgcm support, for being my special CO₂ oracle, and for a nice trip to the Washington D.C. Thanks to Helge Avlesen and Tomas Torsvik for all your encouraging comments, your endless positiveness, and for always smiling when I asked for help and advice. Thank you Øyvind Thiem, for an open door, and your contributions by reading my thesis.

I would like to express a special gratitude to Halvor Utby for patiently fixing my computer, and for explaining my supercomputer problems using simple words and drawings (and for always noticing when I had a rough day). Furthermore, thanks to the rest of the computer guys at Parallab for helpful laptop and supercomputer advice.

Thanks to Alfatih, Håkon, Jon, Kristine, and Maria, my office mates these last years, for putting up with my messy desk, and for contributing to an always friendly office environment. Especially thanks to Maria for all the “around-the-house” breaks, chocolates, and talks! To the rest of the 2nd floor: thanks for nice lunches and for enthusiastically joining all my skiing/ice skating events!

I am also obliged to the rest of my fabulous friends. Thanks for all distractions, nice trips, talks, movie nights, piano and whiskey nights, dances etc. Thanks for your patience in the periods of long working hours, for all the surprise gifts, bring-to-work dinners (so I wouldn't have to spend time picking it up myself), and encouraging comments. You are the best!

I would also like to thank my family for all your support throughout the years and for your belief in me.

And most of all, thanks to Torbjørn for never complaining when I was grumpy, your support whenever I refused to go hiking, and for being the best boyfriend in the world during a challenging period!

Kristin Rygg
Bergen, April 2011

Contents

I	Background and overview	1
	Introduction and outline	3
1	Bottom boundary layers	7
1.1	Vertical structure of the ocean	7
1.2	Boundary layer approximation	8
1.3	Bottom boundary layer	8
1.3.1	Frictional boundary layers	9
1.3.2	Rough surface	11
1.3.3	Modeling the boundary layer	12
1.4	Boundary layer thickness	12
1.4.1	The $u = 0.99U_\infty$ thickness	12
1.4.2	Other measures of the boundary layer thickness	12
1.5	The Reynolds number	13
1.6	Topographic effects	14
1.6.1	Separation point	15
2	Numerical Models	17
2.1	Ocean models	17
2.2	Reynolds Averaged Navier Stokes Models	20
2.2.1	The turbulence closure problem	22
2.2.2	Other assumptions	24
2.2.3	Reynolds averaged equations	25
2.2.4	Hydrostatic versus non-hydrostatic pressure	25
2.3	Options for discretization	26
2.3.1	Horizontal coordinates	27
2.3.2	Vertical coordinates	27
3	The CO₂ problem	31
3.1	Acidification	31
3.1.1	Chemical consequences	32

3.1.2	Biological consequences	32
3.2	Options	33
3.2.1	Geological storage	34
3.2.2	Biological storage	35
3.2.3	Ocean storage	35
3.2.4	Deep-sea sediments	38
3.2.5	Regulations	38
3.3	Transport of CO ₂ into the ocean	39
3.3.1	CO ₂ model	39
3.3.2	Solubilities of CO ₂	43
4	Cold-water corals	45
4.1	<i>Lophelia</i> Pertusa	45
4.1.1	Anatomy	45
4.1.2	Food sources	46
4.1.3	Habitats	46
4.1.4	Threats	48
4.2	Numerical studies	48
4.2.1	Assumptions	49
4.2.2	A model for passive tracers	50
5	Summaries and further work	53
5.1	Summary of the papers	53
5.2	Further work	56
	Acronyms and parameters	59
	Bibliography	65

Part I

Background and overview

Introduction and outline

The ocean covers approximately 70% of the earth's surface [69], and around 97% of all the water on the earth can be found in the ocean [27]. The ocean plays a major role for the climate of the earth, by controlling both the temperature and the weather. Solar radiation is absorbed by the ocean, and due to the large heat capacity of the seawater the upper 2.5 m of the ocean stores as much heat as the entire troposphere [69]. The heat is distributed around the globe by currents, driven by the density differences in the ocean and the wind. In general, the ocean heats the atmosphere and land during the winter and cools the surroundings during summertime. The ocean is also a source of water vapor into the atmosphere.

Uncounted millions of species live in the ocean [119], and life can be found at all depths from the surface and down to the deepest trenches. Coral reefs are one of the main habitats in the ocean, being the home of approximately 25% of all marine life [126]. Humans depend on the ocean for transportation and also for military purposes. In addition, the ocean is a potential energy contributor and a large storage reservoir of chemical components such as CO₂ [119].

There exists historical records of the ocean's importance for at least tens of thousands of years [119]. In the early days, the ocean was mainly considered as an important food source. However, as people started to travel; currents, winds, and depths became the focus of attention. In the mid 1400s with the explorations of the ocean, the large sea voyages contributed to a rapid improvement of the present days maps. In 1768, Captain James Cook began the first out of three voyages to explore the Pacific Ocean [119, 140]. On these trips he systematically measured the longitude, the water depth, the water temperatures, the currents, and the wind speed [119].

The first scientific voyage took place using the old warship the HMS Challenger from 1872 to 1876 [119]. This cruise is considered the start of modern oceanography [119], and during the aforementioned voyage, the physics, chemistry, geology, and biology of the world's ocean were studied. The expedition covered the north and the south Atlantic, the north and the south Pacific, and the southern part of the Indian Ocean [119]. During the Challenger expedition samples were taken of both living creatures, sediments, and rocks from the ocean bottom [119]. In addition, the water depths were measured, and the chemical components in the water column were mapped along with the organic life at different depths [119, 140]. The first depth estimate of the Mariana Trench, 8.185 m, was made on this cruise [119]. The Challenger expedition resulted in identification and classification of 5000 unknown marine species and a sketch of the mean circulation in the ocean [119].

Also at present, marine cruises are an important tool for studying the ocean. Still the instruments have improved. New tools for studying the ocean are de-

veloped and today we also use submarine vehicles, remote sensing, and besides numerical models to study the ocean. Since the early days of oceanography the focus of attention has shifted from the mean circulation in the ocean, to the variability of the mean circulation, regional studies, and process studies. Though our knowledge has increased dramatically since the Challenger expedition, there are still large unknown mysteries as turbulent mixing in the ocean and the connection between large scales and smaller scales in the ocean.

Wilhelm Bjerknes presented in his paper in 1904 seven prognostic equations to forecast the weather [23]. Bjerknes thought the weather could be predicted far into the future by these equations, given suitable initial and boundary conditions. In 1963, Lorenz [82] found that the weather system is chaotic, and small variations in the initial conditions can lead to a different solution [85]. This is due to the non-linear interactions in the Navier Stokes system. Still, these seven prognostic equations are found useful for forecasting both weather systems and also the currents in the ocean, and now form the basis for both atmospheric and oceanic numerical models.

The first numerical ocean model was developed by Kirk Bryan and Michael Cox in the early 1960s [28]. The numerical model was a simple five layer, barotropic model using the rigid lid approximation. With the increasing computer powers, numerical models have now developed into an important tool within oceanography. Numerical models provide a complete description of the entire ocean and continuous estimates of the velocities, temperatures, and salinities. As a comparison, the measurements in the ocean are sparse both in time and space. However, numerical models do not necessarily give us the entire truth, but are only an image of the real ocean. Discretizations of the equations introduce errors to our solution. Additionally we deal with large challenges concerning computational power. The length scales in the ocean are approximately 1/10 of the length scales in the atmosphere, and the timescales are approximately ten times longer [120]. Hence, the computational limitations are much larger for the ocean than for the atmosphere. The equations have to be discretized on a grid and the numerical models are only able to represent processes that are larger than two times the grid size [50]. Processes that are not directly calculated must be parametrized using sub-grid models. Many of the sub-grid models are simple with its principal task to keep the numerical model stable [50]. The ocean is highly turbulent and characterized by three-dimensionality, irregularity, vorticity, and unsteadiness [70]. It is therefore impossible to predict the exact forecast of the turbulent behavior [16]. The lack of physical understanding of turbulence is one of the main challenges of numerical ocean modeling today.

In spite of the challenges, numerical models give us the ability to study processes in the ocean that cover a large specter of time scales and length scales. Coupled atmosphere-ocean models are used to study climate change. Moreover,

ocean models are used for regional studies and also for process studies. Ocean models are an excellent tool for studying the interaction between different scales, and different physical phenomena as tides, mixing, and the large-scale circulation [66].

In this thesis, ocean models are used to study flow near the bottom boundary, both related to transport of CO₂ and passive food particles to corals. Ocean models are in this context a tool to study potential future scenarios of occurrences where it is difficult or illegal to perform corresponding experiments directly in the ocean. The ocean models are also used to explore how small-scale near-bottom processes can affect the settling conditions of cold-water corals and the mixing of chemical compounds in the water column.

Since water transport at the bottom of the ocean is a superior topic in this thesis, Chapter 1 starts out with an introduction to boundary layers. Some basic concepts in ocean models are presented in Chapter 2, before the focus shifts to the specific problems studied in this work (Chapter 3 and 4). Chapter 3 gives an introduction to anthropogenic CO₂ in the ocean, both covering ocean acidification and challenges concerning Carbon Capture and Storage (CCS). Settling conditions for the cold-water coral, *Lophelia Pertusa*, are presented in Chapter 4, along with assumptions and challenges relevant for modeling flow over coral reefs. A summary of all the four papers and prospects of future work are given in Chapter 5. All the relevant variables and abbreviations are listed in the appendix.

Chapter 1

Bottom boundary layers

1.1 Vertical structure of the ocean

In general, the ocean can be divided into three layers determined by the vertical density profile. In the upper layer, the oceanic mixed layer, the energy is supplied into the top few meters through breaking surface waves [27]. The upper layer is affected by wind-driven currents leading to a large vertical velocity shear. In most regions, the surface layer is heated during the summer and cooled during winter-time. The heat flux between the ocean and the atmosphere leads to convection, which is especially effective in high latitudes. Due to the high mixing rate caused by shear and convection, the surface layer is well mixed with near uniform values of the salinities, temperatures, and densities.

At the bottom of the mixed surface layer there is a sharp change in the salinity and/or the temperature gradient, referred to as respectively the halocline or the thermocline. Since the density is determined by the salinity, temperature, pressure, and concentrations of other chemical components [119], the gradient in the salinity and/or temperature profile also causes a rapid change in the density profile. The sharp density gradient is generally entitled “the pycnocline” and leads to a stable water column which inhibits overturning and mixing [27]. The sharp density shift is hence a strong isolation barrier between the mixed surface layer and the deep ocean underneath the pycnocline.

The region below the pycnocline is often called the deep ocean. This region is characterized by a stable, weak, vertical, density gradient. The large-scale currents in the deep ocean are mainly determined by density differences, where water masses with high densities merge towards regions with lower densities, a process often referred to as the thermohaline circulation [27].

In the lowest layer, closest to the bottom, the bottom boundary layer is found.

1.2 Boundary layer approximation

The boundary layer is thin compared to the ambient fluid, hence variations across the boundary layer is assumed much larger than variations in the horizontal direction of the layer [75],

$$\frac{\partial}{\partial x} \ll \frac{\partial}{\partial z}, \quad \frac{\partial^2}{\partial x^2} \ll \frac{\partial^2}{\partial z^2}. \quad (1.1)$$

Here x and z represent the distance in the horizontal and the vertical direction. The following non-dimensional variables [75],

$$\begin{aligned} x' &= \frac{x}{L}, & z' &= \frac{z}{\bar{\delta}} = \frac{z}{L} \sqrt{Re}, \\ u' &= \frac{u}{U_\infty}, & w' &= \frac{w}{\bar{\delta} \frac{U_\infty}{L}} = \frac{w}{U_\infty} \sqrt{Re}, & p' &= \frac{p - p_\infty}{\rho_0 U_\infty^2}, \end{aligned} \quad (1.2)$$

are now introduced, where L represents a characteristic length scale, $\bar{\delta}$ the average thickness of the boundary layer, U_∞ the free flow velocity outside the boundary layer, $Re = \frac{U_\infty L}{\nu}$ is the Reynolds number which will be further discussed in Section 1.5, and p_∞ a reference pressure outside the boundary layer. The horizontal velocity is given by u , the vertical velocity by w , ρ represents the density, and ν the kinematic viscosity. If time dependence and rotation are neglected, the following momentum equations for the boundary layer can be found as $Re \rightarrow \infty$ [75, 142],

$$\begin{aligned} u \frac{\partial u}{\partial x} + w \frac{\partial u}{\partial z} &= -\frac{1}{\rho} \frac{\partial p}{\partial x} + \nu \frac{\partial^2 u}{\partial z^2}, \\ 0 &= -\frac{1}{\rho} \frac{\partial p}{\partial z}, \\ \frac{\partial u}{\partial x} + \frac{\partial w}{\partial z} &= 0. \end{aligned} \quad (1.3)$$

In other words, the pressure, p , is approximately constant across the boundary layer. Since $\frac{\partial}{\partial x} \ll \frac{\partial}{\partial z}$, the vertical velocities, w , within the boundary layer must be small in order to fulfill the equation of continuity.

1.3 Bottom boundary layer

Bottom boundary layers are affected by the free flow velocity outside the boundary layer, U_∞ , and the friction close to the bottom. Due to the bottom friction, the boundary layer is characterized by a large vertical velocity shear. Boundary layers

are hence often well mixed [70]. In the deep ocean the bottom currents are generally weak (of the order of a few cm s^{-1}), leading to very thin boundary layers [70]. In regions with strong bottom currents, the bottom boundary layer can have a thickness of a few tens of meters [70].

1.3.1 Frictional boundary layers

At the solid boundary, the velocity equals zero [75]. This condition is often referred to as the no-slip condition, and applies both for the mean velocity and the fluctuating velocity component. Since the fluctuating velocities also equal zero at the bottom, the Reynolds stresses, $\overline{u'_i u'_j}$, vanish. The no-slip condition generates shear which again is a contributor to turbulence.

In an idealized boundary layer with parallel irrotational viscous flow over a flat bottom, the boundary layer can be divided into different layers depending on the important variables in each region (Figure 1.1).

The viscous sublayer

Very near the wall (within the closest mm) the flow is dominated by viscous effects and bottom stress [75]. The layer is very thin, hence the stress can be considered uniform over the layer, and equal to the wall shear stress, τ_0 [75]. The wall stress

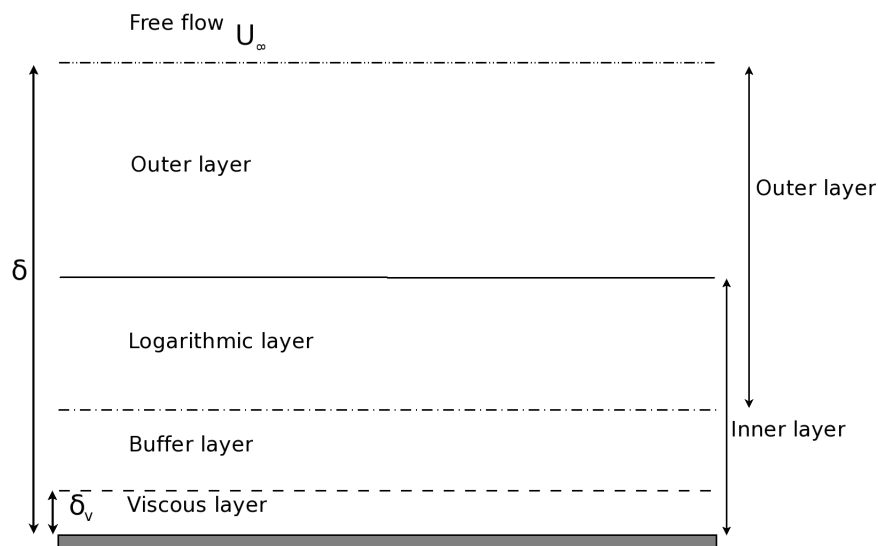


Figure 1.1: The four sublayers within the bottom boundary layer. Note that the relative thickness of the different layers is not correct.

is given by,

$$\tau_0 = \mu \frac{d\bar{u}_x}{dz} , \quad (1.4)$$

where μ is the dynamic viscosity, and \bar{u}_x the horizontal velocity component averaged in the x -direction. Since the stress is considered uniform across the viscous sublayer, integration of Equation (1.4) gives a linear velocity profile. Applying the no-slip condition at the bottom gives,

$$\bar{u}_x = \frac{\tau_0}{\mu} z . \quad (1.5)$$

The thickness of the viscous sublayer, δ_v , is normally of the size of millimeters and can be determined by the following relation $\delta_v \sim \frac{5\nu}{u_*}$ [75]. Here ν represents the kinematic viscosity and u_* the friction velocity. The friction velocity, u_* , can be considered as an expression of the scale of the velocity fluctuations, and can be estimated by [75],

$$u_* \equiv \sqrt{\frac{\tau_0}{\rho}} , \quad (1.6)$$

where τ_0 is the wall shear stress.

The buffer layer

Outside the viscous sublayer the buffer layer is found [75]. Both the Reynolds stress, the friction velocity, and the shear are important parameters in this region [75]. The layer is characterized by large activity. In moderate Reynolds number, most of the turbulent energy is created within the buffer layer [67].

The logarithmic layer

Further away from the solid boundary viscous forces can be neglected. As long as we are not close to the edge of the boundary layer, the flow is not determined by the size of the boundary layer, δ . In this region ($\delta_v \ll z \ll \delta$), the shear, the distance from the wall, and the friction velocity are the important parameters [75]. The vertical velocity gradient in the logarithmic layer can hence be described by the following relation, $\bar{u}_x = f\left(\frac{d\bar{u}_x}{dz}, u_*, z\right)$. Based on Buckingham's Pi theorem, the flow can be described by the two non-dimensional variables [75],

$$\frac{d\bar{u}_x}{dz} \sim \frac{u_*}{z} , \quad (1.7)$$

which can be integrated to give,

$$\frac{\bar{u}_x}{u_*} = \frac{1}{\kappa} \ln z + C_1 . \quad (1.8)$$

The value κ is called the von Karman constant and is considered as an universal constant with the value 0.41, and C_1 is an integration constant which fulfills the boundary condition on the velocity between the logarithmic and the outer layer. The relationship (1.8) is often referred to as “the logarithmic law of the wall” and was derived independently by von Karman in 1930 and Prandtl in 1932 [70]. Laboratory experiments have shown that the thickness of the logarithmic layer is approximately 10% of the thickness of the boundary layer [129].

The outer layer

As we get closer to the outer end of the boundary layer, the normalizing scales are; the boundary layer thickness, δ , and the friction velocity, u_* [70]. In the outer layer the deviation from the free stream velocity has the form [75],

$$\frac{\bar{u}_x - U_\infty}{u_*} = F\left(\frac{z}{\delta}\right). \quad (1.9)$$

The free flow

Some distance outside the boundary layer the flow is in general no longer affected by the wall. In this region the characteristic velocity is the free stream velocity, U_∞ , and the distance from the wall is no longer an important parameter.

1.3.2 Rough surface

In real life the surfaces are seldom smooth, and laminar flow over the bottom are rare. When the surface roughness elements are higher than the viscous sublayer, the flow in the logarithmic layer is determined by the surface roughness, z_0 [75]. The horizontally averaged velocity, \bar{u}_x , can in this case be expressed by the three parameters u_* , z , and z_0 . The velocity can then be described as [75],

$$\frac{\bar{u}_x}{u_*} = \frac{1}{\kappa} \ln\left(\frac{z}{z_0}\right). \quad (1.10)$$

The water masses at $z < z_0$ can be considered stationary. Weatherly and Martin (1978) [138] observed through model studies that the thickness of the boundary layer was relative insensitive to the choice of the roughness parameter. When the surface roughness parameter was increased from 0.03 cm to 1 cm the thickness of the boundary layer was approximately doubled [138].

1.3.3 Modeling the boundary layer

Three-dimensional general circulation models generally do not have sufficient vertical resolution to resolve the logarithmic bottom boundary layer [51]. Approximations are hence needed in order to represent the bottom layer. One of the most popular approximations estimates the bottom stress, τ_b , by a quadratic function of the bottom velocities [24, 51],

$$\vec{\tau}_b = \rho_0 C_D |\vec{U}_b| \vec{U}_b . \quad (1.11)$$

Here ρ_0 represents a reference density and U_b the velocities at the bottom. The drag coefficient, C_D , is defined either by the canonic value of 0.0025 or by a fit to a logarithmic profile,

$$C_D = \max \left(0.0025, \frac{\kappa^2}{(\ln \frac{z_b}{z_0})^2} \right) . \quad (1.12)$$

The distance from the bottom to the middle of the lowest grid cell is given by z_b and z_0 represents the surface roughness. This approximation is valid as long as the closest grid point above the bottom is found within the logarithmic layer [51, 129].

1.4 Boundary layer thickness

The thickness of the boundary layer can be estimated using a variety of methods.

1.4.1 The $u = 0.99U_\infty$ thickness

The simplest measure is to estimate the distance from the wall to the location where the velocity is 0.99 of the free stream velocity [75]. This boundary layer thickness can be noted as δ_{99} . The method is simple but pretty arbitrary, since the thickness of the boundary layer can just as well be chosen as the distance to the point where $u = 0.95U_\infty$ [75].

1.4.2 Other measures of the boundary layer thickness

A more accurate way to measure the thickness of the boundary layer is the displacement thickness, δ^* . In this method a point, h^* , is defined far outside the boundary layer, and the mass flux below this point is calculated for the real flow field. Then the mass flux in a hypothetical friction free flow is estimated. The deviation between the two cases gives the theoretical distance, δ^* , the boundary

would have to be moved outwards in a friction free flow, in order to give the same mass flux as for the real flow [75]. This can be expressed mathematically as,

$$\int_0^{h^*} u \, dz = U_\infty (h^* - \delta^*) . \quad (1.13)$$

Letting $h^* \rightarrow \infty$, Equation (1.13) can be written as,

$$\delta^* = \int_0^\infty \left(1 - \frac{u}{U_\infty}\right) dz . \quad (1.14)$$

It is also possible to estimate the thickness of the boundary layer based on loss of momentum due to the boundary layer [75]. In this case the momentum thickness represents the distance the wall would have to be moved outward in a hypothetical friction-free flow to give the same momentum flux in the real flow as in the friction-free flow below the point h^* [75].

1.5 The Reynolds number

In 1883, Osborne Reynolds demonstrated the difference between laminar and turbulent flow through a tank experiment [112]. In this experiment a thin stream of dye was injected into a pipe filled with flowing water. For sufficient low velocities, the dye followed a straight line. Reynolds increased the velocities in the pipe stepwise, and at some point the dye started to mix with the ambient water, and the tube was filled with colored water instead of a straight line of dye. The dye mixed with the surrounding water through eddies [112]. Reynolds repeated the experiment with varying pipe diameter, velocity, and temperature, and observed that the transition from parallel flow to chaotic flow happened roughly for the same dimensionless parameter. This non-dimensional parameter was presented in his 1895 paper [75, 113],

$$Re \equiv \frac{\text{Inertial forces}}{\text{Viscous forces}} \propto \frac{\rho u \frac{\partial u}{\partial x}}{\mu \frac{\partial^2 u}{\partial x^2}} \propto \frac{UL}{\nu} . \quad (1.15)$$

The Reynolds number, Re , is the ratio of inertial to viscous forces. Here U represents a characteristic velocity, L a characteristic length scale, and ν the kinematic viscosity. The viscous forces acts to suppress turbulence by dissipating the energy in the flow. As the Reynolds number increases, smaller and smaller scales can be found in the flow [75].

For low Reynolds numbers the entire flow is dominated by viscosity, the flow follows parallel streamlines, and is called laminar. For high Reynolds numbers

The pressure gradient can be found from the outer velocity field [75],

$$\frac{dp}{dx} = -\rho U \left(\frac{dU}{dx} \right), \quad (1.17)$$

where x is taken along the surface of the body and U represents the velocity outside the boundary layer. For flow over a topographic height, the velocity increases due to the reduction of the depth. Hence, in an accelerating flow $\frac{dp}{dx} < 0$ at the bottom, leading to [75],

$$\frac{\partial^2 u}{\partial z^2}_{\text{wall}} < 0. \quad (1.18)$$

For decelerating flow, $\frac{dp}{dx} > 0$, and,

$$\frac{\partial^2 u}{\partial z^2}_{\text{wall}} > 0. \quad (1.19)$$

In this case, an inflection point, $\frac{\partial^2 u}{\partial z^2}_{\text{wall}} = 0$, exists somewhere within the boundary layer [75]. The presence of an adverse pressure gradient, $\frac{dp}{dx} > 0$, increases the thickness of the bottom boundary layer [75].

If the adverse pressure gradient generated by the topography is strong enough, negative velocities can occur near the bottom. This phenomenon is called separation and is related to strong vertical movement and rapid growth in the boundary layer thickness [75]. This phenomenon can be explained by the continuity equation,

$$w(z) = - \int_0^z \frac{\partial u}{\partial x} dz. \quad (1.20)$$

Here, the advection contributes to the thickness of the boundary layer [75].

1.6.1 Separation point

The separation point is defined as the boundary between the forward propagating flow, and the backward propagating flow near the wall [75]. At this point, the wall shear stress vanishes, and the region is characterized by large vertical transports due to the meeting flow. In cases where the bottom boundary consists of a sharp step, the separation point is located at the tip of the step [14].

In the separating region, the flow is highly dependent on the Reynolds number. If an analogue is made to flow over a circular cylinder, a stagnant eddy is generated downstream the separation point for Reynolds number less than 40 [75]. As the Reynolds number increases, the flow becomes time dependent and chaotic in the separating region [75].

The boundary layer equations are only valid down to the separation point [75]. Downstream the separation point the boundary layer becomes thick, hence the underlying assumptions for the boundary layer are no longer fulfilled [75].

Chapter 2

Numerical Models

Numerical ocean models are an important tool for studying the ocean. Measurements in the ocean are sparse both in time and space, and numerical models give us the possibility to study large regions with full descriptions of the salinity, temperature, velocity, and pressure fields. The flexibility of the models make them suitable for sensitivity studies to gain more knowledge of the effect and relationship between different parameters. Numerical models also give us the ability to study how different parameters affect the circulation. Besides, models can be used to gain more knowledge of physical processes in the ocean, predict future ocean scenarios, study a wide range of scales, and to explore the relationships and interactions between the different scales.

2.1 Ocean models

Numerical ocean models are mostly based on the same set of equations and basic assumptions. The Navier stokes equations,

$$\frac{\partial \vec{u}}{\partial t} + \vec{u} \cdot \nabla \vec{u} + 2\Omega \times \vec{u} = -\frac{1}{\rho} \nabla p - g\vec{k} + \nu \nabla^2 \vec{u} , \quad (2.1)$$

the equation of continuity of an incompressible fluid,

$$\nabla \cdot \vec{u} = 0 , \quad (2.2)$$

conservation of scalar properties,

$$\frac{\partial \phi}{\partial t} + \vec{u} \cdot \nabla \phi = \kappa_s \nabla^2 \phi + \Phi , \quad (2.3)$$

and an equation of state,

$$\rho = \rho(T, S, p). \quad (2.4)$$

Here \vec{u} represents the velocity components, t the time, Ω the earth's rotation, ρ the density, p the pressure, ν the kinematic viscosity, ϕ the scalar properties such as temperature and salinity, κ_s the diffusivity, Φ a source or sink term of the scalars, T the temperature, and S the salinity. In the rest of the discussion Φ will be set to zero. Hydrodynamic problems can be described with great accuracy based on Equation (2.1) to (2.4) [29].

The discrete versions of the governing equations are an approximation to the real physical problem [75]. By transforming the continuous equations to discrete equations two kinds of errors are introduced, round-off errors and truncation errors. Computers are not able to represent floating numbers accurately [69]. As an example a 64-bit computer represents floating points by around 15 decimal digits [69]. It is possible to increase the accuracy of the calculations by using double precision. However, this will lead to increased computational costs [69]. During sequential operations, round-off errors accumulate.

Truncation errors are generated by the discretization method, and the size of the truncation error can be reduced by using higher order methods [69]. A first order method generally has an error of $O(\Delta x)$ and a n -th order scheme a truncation error of $O((\Delta x)^n)$ [69], where Δx represents the grid size. Another way of reducing the truncation error is to increase the resolution. However, this gives an increased number of sequential operations, leading to a larger accumulated round-off error [69].

The choice of numerical discretization method also affects the solution. The different numerical schemes have different properties regarding stability, monotonicity, and accuracy.

A discrete model is only able to resolve processes that are larger than two times the grid size [50], generating a need for parametrizations of smaller processes. Errors can be introduced by inadequate parametrizations caused by not perfectly understood physical processes [75]. Due to non-linear instabilities, turbulence occur in the flow for high Reynolds numbers [29]. Turbulence is characterized by non-linearity, randomness, and irregularity [70]. Statistical methods can be used to describe turbulence, but at present it is impossible to predict the exact development of the instantaneous turbulent flow [29]. In the ocean, turbulence occurs on a wide range of scales and is generated by shear, waves, and also due to viscous effects near boundaries [29].

Turbulence transports energy from the large scale motion to the viscous scales. Most of the kinetic energy resides in the large scale motion. Non-linear instabilities generate eddies, and the largest eddies extract energy from the mean flow. This energy is gradually transferred to smaller and smaller eddies [75]. As the eddies get smaller, the vertical gradients get sharper, and the eddies get more and more vulnerable to viscosity. Eventually the smallest scales are transferred to heat due to viscous friction [29]. This transect of energy from large to smaller

scales is called the energy cascade.

For high Reynolds numbers there exist an energy spectrum consisting of the energy containing scales, the viscous scales, and the inertial subrange. In the inertial subrange the eddies are independent on both the large scale forcing and the viscosity. In 1941, Kolmogorov [74] presented his famous two-thirds law,

$$E(k_w) \propto \epsilon^{\frac{2}{3}} k_w^{-\frac{5}{3}}. \quad (2.5)$$

Here $E(k_w)$ represents the energy spectrum, ϵ the dissipation rate, and k_w the wave number. This law describes the energy cascade within the inertial subrange, and assumes isotropic turbulence, stationarity, homogeneity, and an infinite Reynolds number.

For small scales, the turbulence is approximately isotropic [75], and the eddies at this scale are not affected by the mean direction of the flow. The dissipation rate, ϵ , depends on the large scales [29]. The two-thirds law gives the basis for the idea that there exist a spectrum equilibrium for turbulence [29]. This assumption is a fundamental idea within all turbulence modeling [29].

Different classes of models can be defined based on how they deal with different scales and turbulent processes.

1. **Direct Numerical simulations, DNS**, solve the governing equations of fluid motions and scalar transport directly without any additional model for turbulence closure. All scales from the Kolmogorov scale, η_k [75],

$$\eta_k = \left(\frac{\nu^3}{\epsilon} \right)^{\frac{1}{4}}, \quad (2.6)$$

and up are resolved by the use of efficient spectral techniques [70]. Here ν represents the kinematic viscosity. In order to achieve correct results, the domain in DNS-simulations must be at least large enough to resolve the largest turbulent eddy in the flow [16] and the grid size should be smaller or equal to the Kolmogorov scale. Direct Numerical Simulations are not an approximation, but can be considered as the exact solution up to the accuracy of the discretization and truncation errors [70]. However, such simulations are highly computationally costly and at present it is only possible to achieve high Reynolds numbers on laboratory scales [70].

2. **Large Eddy Simulations, LES**, resolves the most energy containing eddies, while smaller scales are represented by the use of a sub-scale turbulence closure model [29]. Ideally the model-resolution should be chosen so that the subgrid scales are within the Kolmogorov inertial subrange [70]. In this case the dissipative properties can be parametrized. In LES models

the viscosities and diffusivities in the Navier Stokes equations are replaced by eddy viscosities and diffusivities estimated from the sub-grid turbulence model. The major bottle neck in LES modeling is the turbulence models [70]. It is still a computational costly method, and to model complex three-dimensional flow on a geophysical scale is thus at present not computational achievable [29].

3. **Reynolds Averaged Navier Stokes Simulations, RANS-models**, split the velocities, u , v , w , and the pressure, p , into a mean component and its fluctuations, i.e. $u_i = \bar{U}_i + u'_i$. The Navier Stokes equations are averaged both in time and in space and the goal is to capture the average velocities, average pressure etc. in each timestep. RANS models do not include any random turbulent motion [29], and the turbulent motions are all estimated through sub-scale models and represented by eddy viscosities and diffusivities.

2.2 Reynolds Averaged Navier Stokes Models

The main equations in RANS models are the Reynolds averaged equations of motions, first presented by Osborne Reynolds in 1895 [113]. One of the most important assumptions in ocean modeling is the assumption of an incompressible ocean [69]. By assuming incompressibility, sound waves are filtered out. The equation of continuity of an incompressible fluid can be written as,

$$\frac{\partial u_i}{\partial x_i} = 0, \quad (2.7)$$

using Einstein's notation. If the flow is split into a mean part and the fluctuating part, $u_i = \bar{U}_i + u'_i$, the equation of continuity can be rewritten to,

$$\frac{\partial(\bar{U}_i + u'_i)}{\partial x_i} = 0. \quad (2.8)$$

Taking the mean of Equation (2.8), and simplifying using $\overline{u'_i} = 0$ and $\overline{\bar{U}_i} = \bar{U}_i$, an equation of continuity for the mean flow can be found,

$$\frac{\partial \bar{U}_i}{\partial x_i} = 0. \quad (2.9)$$

To find the Reynolds averaged equations of momentum, we start out by writing the Navier Stokes equation (Equation (2.1) using Einstein's notation,

$$\frac{\partial u_i}{\partial t} + u_j \frac{\partial u_i}{\partial x_j} - f_c \epsilon_{ij3} u_j = -\frac{1}{\rho} \frac{\partial p}{\partial x_i} - g \delta_{i3} + \nu \frac{\partial^2 u_i}{\partial x_j^2}. \quad (2.10)$$

Here (u_1, u_2, u_3) represent the 3D velocity field, δ_{i3} the Kronecker delta function and $f_c = 2\Omega \cos(\theta_e)$ the Coriolis frequency, where Ω represents the rotation of the earth, and θ_e the latitude. The alternating tensor is given by ϵ_{ij3} , ρ represents the density, p the pressure, g the constant of gravity, and ν the kinematic viscosity.

We then split the instantaneous properties in Equation (2.10) into a mean value and its fluctuation,

$$\begin{aligned} \frac{\partial \bar{U}_i}{\partial t} + \bar{U}_j \frac{\partial \bar{U}_i}{\partial x_j} + \frac{\partial u'_i}{\partial t} + u'_j \frac{\partial u'_i}{\partial x_j} + \bar{U}_j \frac{\partial u'_i}{\partial x_j} + u'_j \frac{\partial \bar{U}_i}{\partial x_j} - f_c \epsilon_{ij3} (\bar{U}_j + u'_j) \\ = -\frac{1}{\bar{\rho} + \rho'} \frac{\partial (\bar{P} + p')}{\partial x_i} - g \delta_{i3} + \nu \frac{\partial^2 \bar{U}_i}{\partial x_j^2} + \nu \frac{\partial^2 u'_i}{\partial x_j^2}, \end{aligned} \quad (2.11)$$

take the mean of Equation (2.11) and simplify,

$$\frac{\partial \bar{U}_i}{\partial t} + \bar{U}_j \frac{\partial \bar{U}_i}{\partial x_j} - f_c \epsilon_{ij3} \bar{U}_j = -\frac{1}{\bar{\rho}} \frac{\partial \bar{P}}{\partial x_i} - g \delta_{i3} + \nu \frac{\partial^2 \bar{U}_i}{\partial x_j^2} - \frac{\partial (\overline{u'_i u'_j})}{\partial x_j}. \quad (2.12)$$

Equation (2.12) corresponds to Equation (2.10) except that the instantaneous velocity is now replaced by an average velocity. The extra term on the right hand side of Equation (2.12) represents the Reynolds stresses $\overline{u'_i u'_j}$.

A conservation equation for the scalar properties, ϕ (as salinity, S , and temperature, T) is needed,

$$\frac{\partial \phi}{\partial t} + u_i \frac{\partial \phi}{\partial x_i} = \kappa_s \frac{\partial^2 \phi}{\partial x_i^2}. \quad (2.13)$$

Splitting the scalar properties into $\phi = \bar{\phi} + \phi'$ and taking the mean gives,

$$\frac{D \bar{\phi}}{Dt} = \kappa_s \frac{\partial^2 \bar{\phi}}{\partial x_i^2} - \frac{\partial \overline{u'_i \phi'}}{\partial x_i}, \quad (2.14)$$

where $\overline{u'_i \phi'}$ represents the turbulent flux of the scalar ϕ . In addition, an equation of state is required,

$$\rho = \rho(S, T, P). \quad (2.15)$$

Since the rest of the chapter relates to Reynolds averaged models, the Reynolds averaged properties will in the continuing sections be represented without the overlying bar, i.e. $U_i = \bar{U}_i$.

2.2.1 The turbulence closure problem

To solve Equation (2.12) and (2.14), values are needed for the Reynolds stresses and the turbulent fluxes. The Reynolds stress consists of nine components all varying in time and space. It is possible to derive equations for the Reynolds stresses from the Navier Stokes equations. However, these equations will consist of higher order moments. If one derives equations for the higher order moments they will include terms of even higher orders. This closure problem is often referred to as the turbulence closure problem [69]. In order to close the system, another approach must be chosen.

The simplest way is to assume a linear dependence between the Reynolds stresses and the gradient of the large-scale velocity fields [50],

$$-\overline{u'_i u'_j} = \nu_{x_i x_j} \frac{\partial U_i}{\partial x_j}, \quad (2.16)$$

where $\nu_{x_i x_j}$ is the eddy viscosity. The kinematic viscosity, ν , is a property of the fluid, while the eddy viscosity is a property of the flow. The eddy viscosity consists of nine components depending on time and space [50],

$$\nu_{x_i x_j} = \begin{pmatrix} \nu_{xx} & \nu_{xy} & \nu_{xz} \\ \nu_{yx} & \nu_{yy} & \nu_{yz} \\ \nu_{zx} & \nu_{zy} & \nu_{zz} \end{pmatrix},$$

but is in general simplified to [50],

$$\nu_{x_i x_j} = \begin{pmatrix} \nu_h & 0 & 0 \\ 0 & \nu_h & 0 \\ 0 & 0 & \nu_v \end{pmatrix}.$$

The horizontal eddy viscosity (ν_h) is typically much larger than the vertical values (ν_v) due to the anisotropy in the ocean [50].

The turbulent fluxes of heat and salinity can also be replaced by eddy diffusivities, using the method in Equation (2.16). Introducing eddy viscosities and diffusivities smooths the solution. There exist a wide range of schemes to estimate the eddy viscosities, but at present there is no general agreement of the best turbulence closure model for RANS models.

Subgrid turbulence schemes

The simplest option is to close the system by using constant eddy viscosities and diffusivities. Still, this will not give physical correct results since the amount of mixing depends on among other factors; the horizontal shear and the stratification.

There exists a wide range of parametrizations and some of them are only justified by their ability to produce smooth numerical results [50]. It is often assumed that viscous and diffusive properties can be modeled by the same equations. This assumption could be discussed since for instance monotonicity and positive definiteness are more important for scalar properties than for the momentum equations [50].

Horizontal closure schemes are often based on the Reynolds number, the horizontal resolution, and the rates of stress and strain [50]. An adaptive method to determine the eddy coefficients based on the resolution and the deformation of the velocity field was proposed by Smagorinsky, 1963 [50, 123],

$$\nu_h = (C_M, C_H)\Delta x\Delta y\sqrt{\left(\frac{\partial U}{\partial x} - \frac{\partial V}{\partial y}\right)^2 + \left(\frac{\partial U}{\partial y} + \frac{\partial V}{\partial x}\right)^2}. \quad (2.17)$$

The adjustable constants in this parametrization, C_M , C_H , usually range between 0.05 and 0.2 [50].

The buoyancy frequency, $N^2 = -\frac{g}{\rho_0}\frac{\partial\rho}{\partial z}$, and the Richardson number, Ri, have traditionally been considered important parameters to determine the vertical mixing [50]. The vertical mixing is highly variable over the water column, with large intensity near boundaries, in regions with convection, and low mixing in the interior regions [50]. Some of the less ad hoc methods to estimate the vertical mixing are based on the turbulent kinetic energy [50]. The turbulent kinetic energy, k , can be expressed as,

$$k = \frac{1}{2}\overline{u'_i u'_i} = \frac{1}{2}(\overline{u'u'} + \overline{v'v'} + \overline{w'w'}). \quad (2.18)$$

The equation for the turbulent kinetic energy is found by multiplying the equation for the fluctuating velocities (found by subtracting the Reynolds averaged equation (2.12) from the Navier-Stokes equation (2.10)), with the perturbation velocity (see for instance Haidvogel and Beckmann, 1998 [50] or Kantha and Clayson, 2000 [70]). The conservation of turbulent kinetic energy can then be represented as [50],

$$\frac{\partial k}{\partial t} + U_j \frac{\partial k}{\partial x_j} + \overline{u'_i u'_j} \frac{\partial U_i}{\partial x_j} = -\frac{1}{\rho_0} \frac{\partial \overline{u'_i p'}}{\partial x_i} - \frac{g}{\rho_0} (\overline{u'_i \rho'}) \delta_{i3} - \frac{\overline{u'_i u'_i u'_j}}{\partial x_j}. \quad (2.19)$$

If all lateral derivatives are set to zero, the vertical version of the equation for the turbulent kinetic energy is linearized, and Equation (2.16) is used to represent the Reynolds stresses, the equation for the turbulent kinetic energy can be simplified to [50],

$$\frac{\partial k}{\partial t} = \nu_v \left[\left(\frac{\partial U}{\partial z} \right)^2 + \left(\frac{\partial V}{\partial z} \right)^2 \right] - \kappa_v N^2 + \frac{\partial}{\partial z} \left(\kappa_k \frac{\partial k}{\partial z} \right) - \epsilon. \quad (2.20)$$

Here $P_k = \nu_v \left[\left(\frac{\partial U}{\partial z} \right)^2 + \left(\frac{\partial V}{\partial z} \right)^2 \right]$ is a source term for production of turbulent kinetic energy by vertical shear, and $G_k = -\kappa_v N^2 + \frac{\partial}{\partial z} \left(\kappa_k \frac{\partial k}{\partial z} \right)$ a source term due to buoyancy [50]. The vertical eddy diffusivity is given by κ_v , the vertical diffusivity of the turbulent kinetic energy by κ_k , and ϵ represents the turbulent dissipation rate ($\sim k^3/l$). This equation is the basis for both $k-l$ and $k-\epsilon$ closure schemes. For the former a length scale, l , is used to close the system. Such a method is chosen in the The Mellor Yamada level 2 scheme [50]. In the $k-\epsilon$ scheme, a defined length scale is used to solve an extra equation for the dissipation [50].

Mixing in the ocean

In the deep ocean the circulation is mainly driven by density differences. Ocean mixing determines the water masses, and a correct representation of the mixing is crucial to achieve a realistic circulation in the ocean [66]. In 1966, Munk estimated that the Pacific intermediate and abyssal waters mixed with an average eddy diffusivity of $10^{-4} \text{ m}^2\text{s}^{-1}$ [94]. Though this value was initially an estimate only valid for the abyss, it has been considered as a canonical value valid for the entire interior of the ocean [66]. Later studies of the pycnocline have observed turbulent diffusivities of the order $10^{-5} \text{ m}^2\text{s}^{-1}$ [71, 80]. This value is now considered as the background value in the ocean [48, 66]. Still, near rough topography the turbulent diffusivities are much higher due to breaking internal waves, and the turbulent diffusivities are here measured ranging from $10^{-4} \text{ m}^2\text{s}^{-1}$ to $10^{-3} \text{ m}^2\text{s}^{-1}$ [79, 108].

2.2.2 Other assumptions

In 1903, Boussinesq suggested to include the changes in density only in the gravity term [75]. This approximation is valid when the changes in density is smaller than approximately 3 percent [69], and is an assumption widely used in ocean models. The average potential density in the ocean is 1028 kg m^{-3} [69]. By using the Boussinesq approximation, it is additionally assumed that the dynamic viscosity, the thermal conductivity, and the specific heat may be treated as constants [75]. Sound and shock waves are filtered out, and for compressible flow the full set of equations must therefore be used [75].

Furthermore, the earths rotation is assumed constant, and also the gravity is set to a constant value.

2.2.3 Reynolds averaged equations

The combination of the aforementioned assumptions lead to the following Reynolds averaged equations,

$$\begin{aligned}
\frac{\partial U_i}{\partial t} + U_j \frac{\partial U_i}{\partial x_j} + W \frac{\partial U_i}{\partial z} - f_c \epsilon_{ij3} U_j &= \\
& - \frac{1}{\rho_0} \frac{\partial P}{\partial x_i} + \frac{\partial}{\partial x_j} \left(\nu_h \frac{\partial U_i}{\partial x_j} \right) + \frac{\partial}{\partial z} \left(\nu_v \frac{\partial U_i}{\partial z} \right), \\
\frac{\partial W}{\partial t} + U_i \frac{\partial W}{\partial x_i} + W \frac{\partial W}{\partial z} &= \\
& - \frac{1}{\rho_0} \frac{\partial P}{\partial z} - \frac{\rho}{\rho_0} g + \frac{\partial}{\partial x_i} \left(\nu_h \frac{\partial W}{\partial x_i} \right) + \frac{\partial}{\partial z} \left(\nu_v \frac{\partial W}{\partial z} \right), \\
\frac{\partial U_i}{\partial x_i} &= 0, \\
\frac{\partial \phi}{\partial t} + U_i \frac{\partial \phi}{\partial x_i} + W \frac{\partial \phi}{\partial z} &= \frac{\partial}{\partial x_i} \left(\kappa_h \frac{\partial \phi}{\partial x_i} \right) + \frac{\partial}{\partial z} \left(\kappa_v \frac{\partial \phi}{\partial z} \right), \\
\rho &= \rho(S, T, P).
\end{aligned} \tag{2.21}$$

Here U_i is redefined to represent the horizontal velocities (U, V) and x_i the horizontal coordinate components (x, y).

2.2.4 Hydrostatic versus non-hydrostatic pressure

The pressure, P , in the ocean can be split into three different components,

$$P(x, z, t) = P_\eta(x, t) + P_{int}(x, z, t) + P_{nh}(x, z, t), \tag{2.22}$$

where $P_\eta = g\rho_0\eta(x, t)$ represents the pressure due to the surface elevation, $P_{int} = \int_z^0 \rho(x, z', t) dz'$ the internal pressure, and P_{nh} the non-hydrostatic pressure generated due to internal movements in the fluid.

In large scale studies, the hydrostatic approximation is considered axiomatic to many scientists [84]. Through this simplification it is assumed an exact balance between the vertical pressure gradient and the gravitational force [69],

$$0 = \frac{1}{\rho_0} \frac{\partial P}{\partial z} - \frac{\rho}{\rho_0} g. \tag{2.23}$$

Vertical motions are inhibited by the stable stratification in the ocean leading to small vertical motions and low vertical accelerations [69]. The hydrostatic assumption is valid when the vertical length scale is much shorter than the horizontal length scale, $H/L \ll 1$, and the Froude number, $Fr = \frac{U}{NH}$, is small ($\ll 1$). In 1997, Marshall et al, [84] suggested the non-hydrostatic parameter,

$$n_{nh} = \frac{\gamma^2}{Ri}, \tag{2.24}$$

where $\gamma = h/L$ and $Ri = \frac{N^2 h^2}{U^2}$ represents the Richardson number. The horizontal and vertical length scales are represented by L and h respectively, and the Brunt-Väisälä frequency is given by N^2 . The flow can be considered hydrostatic when,

$$n_{nh} \ll 1 . \quad (2.25)$$

For cases when the hydrostatic assumption is no longer valid, the pressure must be found from the full vertical momentum equation in (2.21). In this case a 3D Poisson equation with homogeneous Neuman boundary conditions must be solved to find the non-hydrostatic pressure [69]. Due to the computational costs, the non-hydrostatic pressure correction should only be included in cases where the non-hydrostatic pressure effects are important and the resolution is high enough to resolve such processes.

2.3 Options for discretization

To transform the partial differential equation into a numerical model, the mathematical model (Equation (2.21)) must be discretized. The finite differences method was first introduced by Euler in the 18th century, and is the oldest numerical method for solving partial differential equations [39]. In finite differences the derivatives are approximated by the use of Taylor series or polynomial fits [39]. Hence, the derivatives are estimated based on neighboring points and are a local approximation [69]. Applied on structured grids, the finite difference method is simple and effective. However, the method does not automatically conserve properties and can only be applied on simple geometries [39].

Finite volume methods use the integral form of the governing equations [39]. The domain is divided into a finite number of subdomains or control volumes, and for each control volume the equations are solved [39]. As the flux that flows into a control volume equals the flux out of the subdomain, finite volume methods are automatically conservative. They are also suitable for complex geometries [39]. However, it is more difficult to implement higher-order methods in finite volume methods compared to in finite difference methods [39].

In the 1960s the finite element method was developed [69]. This method is especially suitable working with complex geometries and when the flow is associated with large spatial variations [69].

Spectral methods are widely used in atmospheric modeling [69]. The spectral method is a global method, where the solution in a spatial point is based on all other points within the model domain [69].

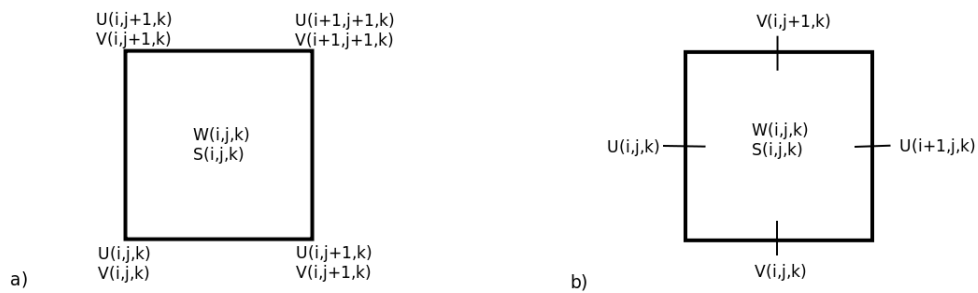


Figure 2.1: A sketch of the Arakawa a) B-grid and b) C-grid.

2.3.1 Horizontal coordinates

There are in general five different ways to arrange the dependent variables S , U , V , and W on a grid. These five arrangements are called the Arakawa grids, named from A to E [69]. Since all five grids consist of the same number of variables, the computing time for each of these arrangements is approximately the same. All the grid types are staggered except for type A, where all the variables are located in the same point. The two most common grids in ocean models are the B- and the C-grid [50, 69]. These two grid types are sketched in Figure 2.1.

The choice of grid determines how well the spatial gradients in the partial differential equation are represented [69]. Averaging over neighboring grid points gives smoothing of the solution and should ideally be avoided [69].

For the B-grid, U and V are calculated in the same grid point (Figure 2.1). This leads to a good representation of the Coriolis term [69], but the calculations of the pressure gradient and convergence/divergence, estimated from the equation of continuity, are compromised [69]. The opposite is the case using the C-grid, pressure gradients and divergence can be calculated directly, but averaging is needed to calculate the Coriolis term [69].

2.3.2 Vertical coordinates

There are several options to discretize the equations in the vertical direction, geopotential coordinates, terrain-following coordinates, and isopycnal coordinates. In this section some advantages and disadvantages of the two former options will be discussed. Examples of two vertical coordinate systems are shown in Figure 2.2.

Geopotential coordinates, or z -coordinate models, use the Cartesian grid. In this case the governing equations can be implemented directly without the use of transformations. When the bottom matrix is discretized into z -coordinates, truncation errors are introduced [50]. The result is a stair-case topography on the

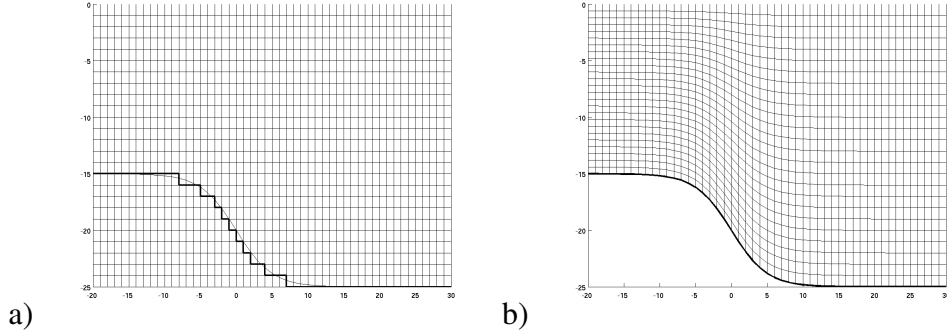


Figure 2.2: a) Geopotential coordinates (z -coordinates) and b) terrain following coordinates (σ -coordinates).

slopes, which can generate false vertical transports and spurious mixing near the steps [69].

Using terrain-following coordinates, the Reynolds averaged equations are transformed using the standard σ -transformation,

$$x^* = x, \quad y^* = y, \quad \sigma = \frac{z - \eta}{H + \eta}, \quad t^* = t. \quad (2.26)$$

Here σ varies between 0 and -1. The σ -coordinates have the value 0 at the surface and -1 at the bottom. The number of vertical layers in the ocean are the same over the entire domain. In cases with steep slopes, there can be large variations in the thickness of a given σ -layer in the deep and the shallow regions.

Since the terrain-following coordinates follows the bottom topography, resolving the boundary layer only requires enough layers located close to the bottom [69]. As for the z -coordinates, this is a larger challenge since the thickness of each vertical layer is uniform over the entire domain. A sufficient resolution of the boundary layer might hence require a large number of inactive cells [50].

The kinematic boundary condition of no flow through the bottom is easy to implement using terrain-following coordinates, since the lowest σ -layer follows the bottom. For models with geopotential coordinates there will be an error in the flow field due to the truncation error generated by the step-wise bottom. This can lead to artificial vertical transports [69].

Using z -coordinate models, the internal pressure gradient is calculated accurately along the exact horizontal lines [69]. Terrain-following models have problems with spurious mixing due to errors in the estimate of the internal pressure gradient. As the pressure equation is transformed into σ -coordinates, the x -component of the internal pressure may be written as follows [19],

$$\frac{\partial \rho}{\partial z} \Big|_z = \frac{\partial \rho}{\partial x} - \frac{\sigma}{H} \frac{\partial H}{\partial x} \frac{\partial \rho}{\partial \sigma}. \quad (2.27)$$

In situations with steep topography the two terms on the right hand side may be large, comparable in magnitude, and of opposite signs [19]. This can lead to large errors when the internal pressure is estimated [19]. The error in the estimate of the internal pressure first generates false velocities (first order error) [87]. The error in the velocity field generates steering in the water masses, leading to a compensating error in the density field (second order error). Many methods have been suggested to reduce the errors in the internal pressure gradient in σ -coordinate models. Some of these are; subtracting the average density [45], adding viscosity [87], calculating the internal pressure by higher order methods [86], and rotating the grid [130]. It has also been proposed to make two estimates of the internal pressure gradient in z -coordinates and later choose the lowest estimate. In the cases where the two estimates are of opposite signs, the internal pressure gradient is corrected to zero [124]. Lately the perfectly balanced σ -method has been proposed by Berntsen, 2011 [21], where the σ in Equation (2.27) is adjusted such that the internal pressure gradient equals zero in cases where the density field is only a function of depth, $\rho = \rho(z)$.

However, in spite of a large scientific focus for the last 40 years, the problem regarding internal pressure in σ -coordinate models is still not solved. Especially for cases with steep topography and stratification, the false velocities due to errors in the internal pressure gradient might be large [19].

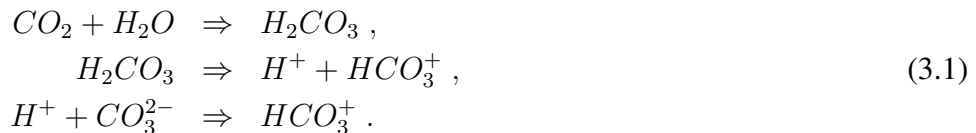
Chapter 3

The CO₂ problem

The CO₂ levels in the atmosphere have increased by 35% over the last two centuries [37], and have led to a raised concern that the increased CO₂ concentrations may lead to global warming and an acidified ocean.

3.1 Acidification

Due to the enhanced atmospheric CO₂ levels, there is a net transport of approximately 2 Gt carbon per year into the ocean [121]. If one considers a timescale of centuries, around 75% of the CO₂ released into the atmosphere will be absorbed by the ocean [6]. CO₂ is rapidly transferred from the atmosphere to the ocean by breaking waves and air bubbles which are entrained into the wind-induced layer [101]. The CO₂ is dissolved in the water in the following manner [101],



Thus, as the concentration of CO₂ in the ocean increases there is a net increase in the bicarbonate concentration, HCO₃⁺, and a reduction in the concentration of carbonate ion, CO₃²⁻. In the ocean, as little as 1% of the carbon can be found as molecular CO₂, and more than 90% as bicarbonate ion (HCO₃⁺) [101]. The average global pH in the surface layer is 8.2±0.3 [109], and the transport of CO₂ into the surface layer has led to a pH reduction of approximately 0.1 units since the industrial revolution, corresponding to an increase in acidity of 30% [135]. This pH reduction has been measured for instance in the Bermuda Strait [15] and the Canary Islands [118]. Model studies show that in time the acidified water will affect the entire water column [30]. The CO₂ is transported into the deep ocean in regions with downwelling and deep water formation and also through

the biological pump. In the biological pump, CO₂ is transported into the deep ocean as dead debris after first being taken up by the ocean biota [109].

3.1.1 Chemical consequences

Calcifying organisms highly depend on the CaCO₃ saturation,

$$\Omega_{sat} = \frac{[Ca^{2+}][CO_3^{2-}]}{K_{sp}^*}, \quad (3.2)$$

where [Ca²⁺] and [CO₃²⁻] represent the concentrations of respectively the calcium and the carbonate ion. The solubility product, K_{sp}^* , depends on the salinity, temperature, pressure, and the mineral phase (aragonite or calcite) [34]. In regions where Ω_{sat} is less than 1, the skeletons and the shells of the calcifiers will start to dissolve. The saturation horizon is defined as the depth where $\Omega_{sat} = 1$ [109]. As more and more CO₂ is taken up by the ocean, the concentration of carbonate ion is reduced, and the saturation horizon rises towards the surface. Estimates have shown that due to anthropogenic CO₂, 70% of the present-known cold-water corals will most likely be located in waters which are undersaturated with respect to aragonite by year 2100 [49, 103].

A rise in CO₂ concentrations will most likely also affect the availability of nutrients and toxins in the ocean [109].

Reduced pH values lead to decreased sound absorption for low frequencies ranging from 0 - 10 kHz [54, 62]. Between the industrial revolution and year 2100 the pH in the surface layer is expected to be reduced by up to 0.6 pH units, leading to a reduction in the sound absorption of up to 60% [62]. Such a change might have consequences for the marine life and also for acoustic measurements [62].

3.1.2 Biological consequences

The pH decrease of -0.6 predicted for year 2100 gives the largest observed pH shift in the ocean for at least 420 000 years [109]. In addition, the pH change is at least 100 times more rapid than previous occurrences over the same period [53, 109].

Photosynthetic marine organisms, as for instance phytoplankton, are the most important contributors to the marine food web, consisting of more than 99% of the organic matter [109]. Consequences for the marine microorganisms will hence have a large effect on the food access in the ocean. Many experiments have studied how elevated CO₂ concentrations in the ocean will affect the level of photosynthesis. In most of the experiments, the rate of photosynthesis is reduced by less

than 10% when exposed to atmospheric CO₂ concentrations two times higher than today [17, 109]. Still there are some exceptions. *Emiliana huxlyi* experienced an increase of approximately 50% in the level of photosynthesis when the CO₂ concentrations were doubled [117, 109]. Further studies are still needed, since it is possible that the phytoplankton might be more affected by indirect factors of acidification as changes in the availability of nutrients and toxins.

Marine animals

Raised CO₂ concentrations will lead to lower oxygen levels in the ocean, making it more difficult for the mammals to obtain oxygen from the seawater [109]. The changed chemical properties of the water might also lead to acidification of body tissues and fluids [65] and affect the bloods ability to carry oxygen [109]. These factors might lead to higher mortalities among the mammals. Fishes which live in a CO₂ rich environment are exposed to an increased risk of cardiac failure [65]. Especially squids and deep sea fish are sensitive to pH changes. Experiments with freshwater fish have shown reduced activity of the sperm when exposed to lower pH values [63]. In addition the egg production of copopods decreased as the pH values in the ambient water were reduced from 8 to 6 [76, 77].

Calcifying organisms depend on the aragonite/calcite saturation. Langdon et al, 2000 [78] found a relationship between lower calcification rates and reduced saturation of aragonite and/or calcite. This result is confirmed by almost all experiments to date. When exposed to reduced saturation rates, the calcifiers may keep their physical extent by decreasing the density of their skeleton [55]. However, this will make them more vulnerable for erosion and give them less ability to absorb wave energy [55]. Another option for the calcifiers is to invest more energy into calcification, leading to less resources available for reproduction [55]. Hence, though the calcifiers may adapt to a more CO₂ rich environment, acidification leads to a chronic stress for the calcifying organisms, making them less resistible to diseases, bleaching, and other threats [55].

3.2 Options

There are three main alternatives to decrease the CO₂ concentrations in the atmosphere; reduce the use of energy, switch from carbon energy sources to carbon free sources, and/or introduce more carbon sinks [10]. It is unlikely that the worlds energy need will be reduced in the near future, thus options to provide a bridge into a carbon free future are needed.

Pacala and Socolow, 2004 [106] suggested several ways to reduce the CO₂ releases into the atmosphere by using technologies that are already feasible today.

One proposed possibility is CO₂ storage. There are several ways to store CO₂; in geological formations, through biology, directly in the ocean, or by storing CO₂ in deep-sea sediments.

3.2.1 Geological storage

Old, depleted oil and gas reservoirs, and saline aquifers have huge potential storage volumes for CO₂. In 1996, Statoil started injecting CO₂ into the Utsira formation due to the high offshore CO₂ taxes in Norway. This was the beginning of a new approach to reduce the CO₂ emissions [18]. Since then similar projects have been undertaken also in Algeria and in Canada, and at present more than 20 million tons CO₂ have been stored [18]. However, in order to significantly reduce the CO₂ emissions using geological storage, the injection rates must be multiplied.

Suitable storage sites should be characterized by large pore volumes, high connectivity, and be covered by an extensive seal [18]. Moreover, the basin should be located at least 800 m below the seabed [18]. The high permeability and porosity makes high injection rates feasible [18]. CO₂ is trapped in the formation by four different mechanisms. The main barrier is a thick seal at the top of the formation, like for instance caprock. This seal should have a low permeability and a high capillary entry pressure to avoid escape of CO₂ from the formation [18]. As the supercritical CO₂ is injected, the original fluid in the formation is depleted as CO₂ propagates through the porous rock. The injected CO₂ is later displaced by pore water. During this process some CO₂ will be trapped as small droplets due to capillary forces, often referred to as residual-phase trapping [18]. In time, CO₂ dissolves in water. As the CO₂ is dissolved, the density of the pore water increases, making the potential of escape by buoyant forces smaller [18]. CO₂ can also react directly with minerals leading to storage by mineral trapping [18].

At the temperature and pressure conditions relevant for geological storage, the CO₂ will be buoyant and will therefore rise towards the structural barrier after injection. Geological formations have proved their capability of storing buoyant fluids for millions of years. However, many of these formations are penetrated with several wells, which are possible pathways for leakage [98]. Besides, leakages can occur by for instance over-pressurization of the caprock during injection, leakage through faults, or by slow seepage through the low permeable seal [98].

Already in 2003, Celia and Bachu [31] focused on the leakage problem related to geological storage. In order to protect existing and future energy sources, the shallow ground water, mineral sources, and to also avoid leakage back to the atmosphere, the risk of leakage must be evaluated [31, 98]. In this context, both the global effect of leakage back to the atmosphere and potential local environmental consequences are of importance. For each storage site, the maximum leakage rate should therefore be estimated along with a probability of leakage. These mea-

asures should be used to evaluate the ecological risks of storage against the risk of no action [31].

Based on data relevant from an enhanced-oil-recovery field in USA, Kano et al, 2009 [68] did numerical simulations of seepage into the ocean. The seepage rate used was 3800 tons per year leaking over an area covering 2 times 200 m. The CO₂ leakage was modeled on the shape of CO₂ droplets, and Kano et al, 2009 [68] found that all the CO₂ was dissolved in the water column before it reached the surface. Furthermore they found that the increase in pCO₂ was lower than 500 μatm, a value assumed low enough to avoid biological impact [68].

3.2.2 Biological storage

Carbon is absorbed in the vegetation through the photosynthesis [99]. Though some CO₂ is released back into the atmosphere by respiration, there is a net storage of CO₂ [121]. Nilsson and Schopfhauser, 1995 [97] estimated that if the worlds forests were extended to its maximum limit by 345 million hectares, a CO₂ reduction of 1.5 Gt carbon per year could be achieved. This is less than 20% of the yearly emissions of CO₂ to the atmosphere [99]. In addition such extensive planting of trees would exclude large landmasses for agriculture.

Another option is to fertilize the forest and ocean to increase the uptake of CO₂ from the atmosphere. However, manipulating the biological production by fertilization is considered a risky project since the consequences for the ecosystems are unknown [2].

3.2.3 Ocean storage

Already in the 1970s the ocean was suggested as a good storage facility for CO₂ by Marchetti, 1977 [83]. The ocean covers approximately 70% of the surface of the earth, and there is an equilibrium between the CO₂ levels in the ocean and the atmosphere [64]. The net result if the CO₂ is first released to the atmosphere or the ocean will eventually be the same. However, in order to reach an equilibrium between the ocean and the atmosphere, thousands of years is required since the deep ocean is separated from the atmosphere by the pycnocline. Injecting CO₂ directly into the deep ocean will keep the CO₂ away from the biologically active surface layer and also overcome the time related bottleneck due to the pycnocline [5].

In the ocean, CO₂ is found in gas phase until approximately 500 m depth (see Figure 3.1). Below 500 m depth the CO₂ will be in liquid phase, but be less dense than seawater [64]. Due to the higher compressibility of CO₂ compared to seawater, the density of liquid CO₂ will be higher than the ambient seawater at approximately 3000 m depth [64].

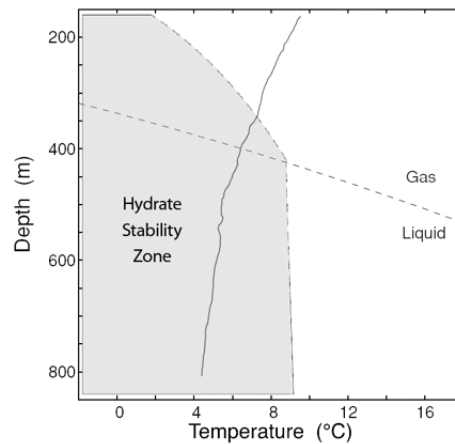


Figure 3.1: Temperature and pressure conditions for the different phases of CO₂. The figure is taken from Brewer et al, 2004 [26], *Small Scale Field Study of an Ocean CO₂ Plume*, Journal of Oceanography, Figure 1, and is reprinted with the kind courtesy of Springer Science and Business Media.

Several methods are proposed to inject CO₂ into the ocean. The storage time and the pH reduction is to a large extent dependent on the phase (gaseous/liquid), the method (ship, fixed pipeline), and the depth of injection (500-4000 meters) [5]. The CO₂ can be stored as; dry ice, a dense plume, a CO₂ lake, and by two different injection methods, a fixed pipe and a droplet plume [5, 64].

Two injection methods have been considered the most favored options. One possibility is to inject CO₂ through a fixed pipe at more than 3000 m depth. At this depth the CO₂ will be in liquid phase and denser than the ambient water. The liquid CO₂ will sink along the bottom to trenches in the topography and create lakes [64]. In regions of cold temperatures and high pressures, the CO₂ is within the hydrate stability zone (Figure 3.1). Hydrate formation increases the insulation between the CO₂ and the seawater and reduces the dissolution. Still, the hydrate formation will not lead to complete insulation from the seawater. The hydrate crystals will continuously be renewed [91]. Hydrate formation has been observed through both laboratory experiments [9] and deep ocean experiments [25]. At depths deeper than approximately 4000 meters, the liquid CO₂ will be denser than the hydrate due to the temperature and pressure conditions.

A second option is to inject liquid CO₂ at depths ranging between 1000 and 1500 meters. At such depths the liquid CO₂ will be diffused as droplets [4]. These droplets will rise slowly, and be gradually reduced in size before they dissolve in the water. The CO₂ enriched seawater is more dense than the ambient water and will hence sink. As the dissolved CO₂ is affected by turbulence and currents, the plume becomes more diluted and spread [4, 5]. The dispersed CO₂ will lead to

reduced pH values near the injection point. The droplet method will affect larger water masses than the lake scenario, but will have smaller pH reductions [64].

In order to determine if ocean storage is acceptable one must consider the environmental consequences. These consequences should be divided into two subgroups; environmental impacts on a global scale and on a local scale. On a global scale, leakage back to the atmosphere and acidification of the productive surface layers are the most important factors. On a local scale, ocean sequestration will lead to reduced pH values and can affect the marine biota near the injection point.

In 2004, eight different ocean models were used to evaluate the efficiency of ocean storage [102]. In order to evaluate the success of ocean sequestration, the measure “global efficiency” was introduced. Global efficiency is defined as the total mass of injected CO₂ that is still located in the ocean at a reference time, divided by the total mass of injected CO₂ since the beginning of the simulation [102]. In general, the injection depth increases the storage time and the storage efficiency [5], and CO₂ injected beneath the permanent pycnocline has a higher residence time than CO₂ injected above the pycnocline. If CO₂ is injected at 3000 m depth, the global efficiency is evaluated to 97% or higher 100 years after injection [102]. After 500 years, 48 to 82% of the injected CO₂ is still located in the ocean [102]. The residence time highly depends on the general ocean circulation. When CO₂ is injected at 1500 and 3000 m depth, the global efficiency is higher for the Pacific sites than for sequestration sites in the Atlantic or the Indian Ocean [102]. Major ocean CO₂ sinks as the warm western currents (for instance the Gulf Stream) and regions of deep water formation (the North Atlantic and the Southern Ocean) are considered particularly suitable for CO₂ storage, with residence times of up to thousands of years [5]. Regions with upwelling are on the contrary not good choices as sequestration sites [5].

Orr, 2004 [102] estimated the pH at the injection sites to be reduced by 0.1 to 2 pH units during injection. These simulations are coarse scale simulations with horizontal resolutions of 1.5 to 5 degrees [102]. The pH reductions might hence be dramatically higher as local variances are resolved.

CO₂ injection in the deep ocean is expected to have environmental consequences [137]. Deep-water organisms are used to smaller fluctuations in the pH values compared to the organisms that live near the surface, and might therefore be more sensitive to pH changes [7]. The consequences for the marine biota depend on the pH change and the duration of the exposure to acidified water masses [7]. Elevated CO₂ concentrations lead to increased stress levels for the jeopardized beings. However, many organisms have built in methods to compensate for large CO₂ concentrations, making the toxic effects of reduced pH values reversible [7]. Vetter and Smith, 2005 [137] exposed scavengers to moderately elevated CO₂ concentrations at the Loihi vent for one hour. After 30 seconds, the scavengers

were swimming with an increased speed. Ten minutes later, 90-95% of the beings were immobile due to narcotic effects from the CO₂ plume [137]. After one hour, the scavengers were relocated from the acidified water masses, and 30 minutes after removal all creatures were swimming again [137]. Vetter and Smith, 2005 [137] also observed that mobile scavengers avoided baits located in CO₂ enriched waters. In contrast, Tamburri et al, 2000 [127] observed a hagfish which repeatedly approached bait in a CO₂ plume, lost consciousness and sank to the bottom, woke up again, only to repeat the procedure. Barry et al, 2004, 2005 did long term experiments on deep sea meiofauna where organisms were exposed to liquid CO₂ at 3600 m depth [12, 13]. In their experiment they measured a pH change of up to -1.6 pH units near the liquid CO₂, leading to a high mortality rate for the meiofauna surrounding the CO₂ pools (>90%) [12]. The organisms living in the sediments in the near vicinity of the pools experienced an even more severe mortality rate than the organisms in the water column [12]. Also the deep-sea species exposed to more diluted water masses (pH changes from 0.1 to 0.2 pH units below normal) had higher mortality rates than at the control sites [12].

3.2.4 Deep-sea sediments

The sediments of the ocean are a potential environment for CO₂ storage. If CO₂ is injected into marine sediments at temperatures below 5°C and pressures higher than 3 MPa, CO₂ hydrate will provide a seal to prevent escape from the sediments [73]. If in addition CO₂ is injected several hundred meters into the sediments below a 3000 m deep water column, the injected CO₂ will have a higher density than the ambient pore water [56]. In this case, liquid CO₂ will be separated from the marine environment by two distinct barriers; a hydrate layer and the negative buoyancy [56]. If one considers a timescale of thousands of years, the CO₂ will also dissolve in the pore water [56].

House et al, 2006 [56] claim that the potential storage volumes outside the economical zone of the US can be considered boundless. However, the consequences of depleted pore water due to injected CO₂ should be further studied [56]. Still, storage in deep-sea sediments is a potential sequestration method, with hopefully small environmental consequences, and less need for monitoring than the geological storage alternative [56].

3.2.5 Regulations

Storage of CO₂ is regulated by international laws. In 1972, the London Convention prohibited dumping of waste to the ocean without permission from a national authority (www.londonprotocol.imo.org). Moreover, the North-East Atlantic is regulated by an international agreement to protect the marine environment (the

OSPAR Convention). Originally, neither the London Convention nor the OSPAR Convention allowed for storage of CO₂. However, both commissions opened up for CO₂ storage as a remedy to reduce the CO₂ emissions to the atmosphere in 2007 [81, 105]. The EU also have regulations for Carbon Capture and Storage, CCS [107].

OSPAR came with a statement to prohibit ocean storage in the water column and on the seabed in 2007 [104]. This decision was founded by concern for the marine environment. OSPAR considered ocean storage harmful for the marine ecosystem, and not a sustainable solution to avoid climate change [104].

Both the OSPAR Convention and the London protocol give some restrictions for geological storage of CO₂. It is only allowed to store pure CO₂. Thus, other substances can not deliberately be added to the CO₂ plume [105]. In the pre-injection phase, the company should estimate the storage volume of the formation and demonstrate that the barriers are sufficient to last for long-term storage. A risk assessment should be performed addressing; possible pathways for leakage, potential risks for the ocean, and besides a plan for monitoring [105]. The plan should include monitoring procedures both in the injection phase and in the infinite period after closing down the injection wells. The risk assessment should focus on both long-term and short-term processes [105]. In addition, a thorough study of the marine environment should be done [105]. In the pre-study, the ocean currents and also the seafloor above the storage site should be mapped. The study should include measurements of the natural fluxes of CO₂ on the seabed, the chemical characteristics of the seawater, the natural concentrations of nutrients, and a study of the composition, structure, and dynamics of the biological communities [105]. The company should also report back to OSPAR in all phases, both during planning, in the injection phase, and also in the period of monitoring after injection, all this in order to secure a safe storage procedure for CO₂.

3.3 Transport of CO₂ into the ocean

At approximately 400 m depth, hydrate will form at the interface between CO₂ and seawater [64]. CO₂ hydrate is the nonstoichiometric crystalline phase of CO₂ and water [134], and consists of water molecules that form a cage around each CO₂ molecule [64]. The water cage isolates the CO₂ from the seawater and consequently reduces the dissolution rate. The hydrate molecules are constantly renewed. CO₂ hydrate is approximately 10% denser than typical abyssal waters [134].

3.3.1 CO₂ model

Mori and Mochizuki, 1997 [90] presented a model for a steady, solid, uniform hydrate film isolating liquid CO₂ from the ambient water. The following description is mainly based on their 1997 paper. The fundamental basis of Mori and Mochizuki's model is mass conservation of a hydrate layer in steady state [90]. The mass conservation can be expressed by [91],

$$\dot{\eta}_{wh} + \dot{\eta}_{wg}|_{z=0} = n(\dot{\eta}_{gw}|_{z=\delta} + \dot{\eta}_{gh}) , \quad (3.3)$$

where $\dot{\eta}$ represents spatially averaged molar fluxes. The molar flux of water that flows through the hydrate film is given by $\dot{\eta}_{wh}$, and $\dot{\eta}_{gh}$ represents the average molar flux of CO₂ that flows through the hydrate layer (Figure 3.2). The flux of CO₂ that dissolves into the water phase is represented by $\dot{\eta}_{gw}|_{z=\delta}$, and the flux of water into the liquid CO₂ beneath the hydrate layer is given by $\dot{\eta}_{wg}|_{z=0}$ [91]. The hydration number is represented by n , and is set to 5.75. The left side of Equation (3.3) represents the net flux of water which contributes to hydrate formation on the CO₂-side of the hydrate film, and the right hand site represents the release rate of CO₂ hydrate molecules on the water-side of the hydrate layer [91]. Formation of hydrate is controlled by the water permeation through the capillaries, and the dissolution of hydrate is controlled by diffusion and transport of the CO₂/guest molecules on the water-side of the hydrate film [90]. Since dissolution of hydrate is controlled on the water-side of the hydrate film, the term $\dot{\eta}_{wg}|_{z=0}$ is neglected.

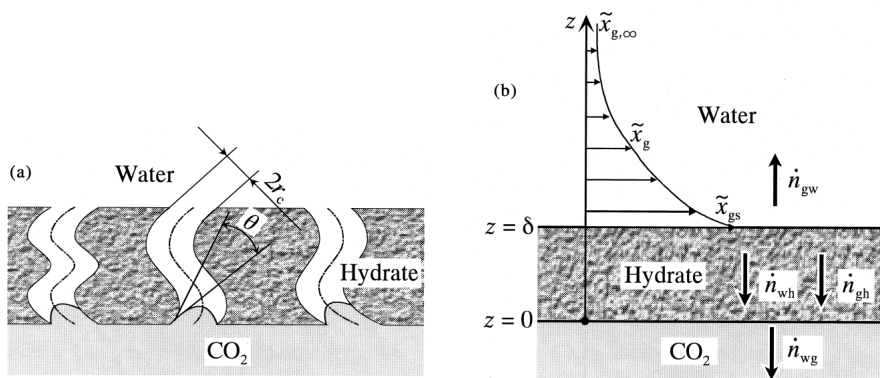


Figure 3.2: A sketch of a) the internal structure of the hydrate layer and b) the transport through and away from the hydrate layer. The figure is reprinted from Mori and Mochizuki, 1998 [91], *Clathrate hydrate formation at the interface between liquid CO₂ and water phases - a review of rival models characterizing "hydrate films"*, Energy Conversion Management, 38 (20), Figure 1, with kind permission from Elsevier.

Mori and Mochizuki, 1997 [90] assume that all flow through the hydrate layer occur through the capillaries. All the capillaries are described using the same radius, r_c . The length of each capillary are $\tau\delta_h$, where τ represents the tortuosity (≥ 1), and δ_h the thickness of the hydrate layer. Inside the capillaries there are no formation and dissolution of hydrate [90]. Mori and Mochizuki, [90] assume that the flow in the capillaries can be expressed as Hagen-Poiseuille flow [141]. By this assumption it is additionally assumed that the flow through the capillaries is laminar, viscous, and incompressible. The volumetric flow, $\dot{V}_{mix_{cap}}$, of saturated water with CO₂ can therefore be expressed as,

$$\dot{V}_{mix_{cap}} = \int_0^{r_c} u \, 2\pi r \, dr = \int_0^{r_c} \frac{(r^2 - r_c^2)}{4\mu_{mix}} \frac{dp}{dz} 2\pi r \, dr = \frac{\pi r_c^4}{8\mu_{mix}} \frac{\Delta P}{\tau\delta_h}, \quad (3.4)$$

where $-\frac{dp}{dz}$ is substituted by the pressure drop over the entire length of the capillary through the hydrate layer. The water in the capillaries are assumed saturated with guest species (CO₂), and the dynamic viscosity of the saturated water with CO₂ is represented by μ_{mix} .

The capillary pressure is the driving force for sucking water into the capillaries. We assume that the capillary pressure can be described using the Young-Laplace equation, $\Delta P = 2\sigma_{mix}\cos(\theta)/r_c$. Here σ_{mix} represents the surface tension between water and liquid CO₂, and θ the contact angle of the capillary wall on the water-side (see Figure 3.2 a)). The total molar flow rate of saturated water of CO₂ through a capillary can then be expressed by [90],

$$\dot{N}_{mix_{cap}} = \dot{V}_{mix_{cap}} \frac{\rho_{mix}}{M_{mix}} = \frac{\pi r_c^3 \sigma_{mix} \cos(\theta)}{4M_{mix} \nu_{mix} \tau \delta_h}, \quad (3.5)$$

where ν_{mix} represents the kinematic viscosity of CO₂. The effective molar mass, M_{mix} , of the water saturated with CO₂ is defined as,

$$M_{mix} = M_w(1 - \tilde{\chi}_{gs}) + M_g \tilde{\chi}_{gs}. \quad (3.6)$$

The molar mass of water and CO₂ are given by M_w and M_g respectively. The mole fraction of saturated water with CO₂, $\tilde{\chi}_{gs}$, is defined as the ratio of the number of moles with dissolved CO₂ in the solution over the total number of moles in the mixture [122],

$$\tilde{\chi}_{gs} = \frac{\text{amount (mol) of CO}_2}{\text{amount (mol) of seawater} + \text{amount (mol) of CO}_2}. \quad (3.7)$$

We now want to transform the molar flow rate, $\dot{N}_{mix_{cap}}$, for each capillary to a spatially averaged molar flux, \dot{n}_{mix_h} , for flow through the hydrate film. The molar flow through a capillary is therefore multiplied with a number n_{cap} which represents the density of capillaries in the hydrate layer. The relationship between

n_{cap} and the porosity of the hydrate film, ϵ_p , can be expressed as $\epsilon_p = \pi r_c^2 \tau n_{cap}$ [90]. This leads to an average molar flow rate of saturated water through the hydrate layer, expressed as,

$$\dot{n}_{mix_h} = \dot{N}_{mix_{cap}} n_{cap} = \frac{\sigma_{mix} \cos(\theta) r_c \epsilon_p}{4M_w \nu_w \tau^2 \delta_h} . \quad (3.8)$$

This expression can be split into the molar flux of pure water flowing through the hydrate layer,

$$\dot{n}_{wh} = \dot{n}_{mix_h} (1 - \tilde{\chi}_{gs}) = \frac{\sigma_{mix} \cos(\theta) r_c \epsilon_p}{4M_{mix} \nu_{mix} \tau^2 \delta_h} (1 - \tilde{\chi}_{gs}) , \quad (3.9)$$

and the molar flux of CO₂,

$$\dot{n}_{gh} = \dot{n}_{mix_h} \tilde{\chi}_{gs} = \frac{\sigma_{mix} \cos(\theta) r_c \epsilon_p}{4M_{mix} \nu_{mix} \tau^2 \delta_h} \tilde{\chi}_{gs} = \dot{n}_{wh} \frac{\tilde{\chi}_{gs}}{1 - \tilde{\chi}_{gs}} . \quad (3.10)$$

According to Bird et al, 2002 [22], the mass transfer from the hydrate layer and into the water column can be expressed by,

$$\dot{n}_{gw}|_{z=\delta_h} = k_{gw} (\tilde{\chi}_{gs} - \tilde{\chi}_{g\infty}) + \tilde{\chi}_{gs} (\dot{n}_{gw}|_{z=\delta_h} - \dot{n}_{wh}) . \quad (3.11)$$

Here $\tilde{\chi}_{gs}$ represents the saturated water with CO₂ at the interface between the hydrate layer and the ambient water, $\tilde{\chi}_{g\infty}$ the mole fraction of CO₂ further up in the water column, and k_{gw} a mass transfer coefficient given in moles s⁻¹m⁻². Combining Equation (3.11) with Equation (3.9) leads to,

$$\dot{n}_{gw}|_{z=\delta_h} = \frac{1}{1 - \tilde{\chi}_{gs}} \left[k_{gw} (\tilde{\chi}_{gs} - \tilde{\chi}_{g\infty}) - \frac{\tilde{\chi}_{gs}}{1 - \tilde{\chi}_{gs}} \dot{n}_{wh} \right] . \quad (3.12)$$

The mass transfer coefficient, k_{gw} , can be expressed as,

$$k_{gm} = K_m \frac{\rho_{mix}}{M_{mix}} , \quad (3.13)$$

where K_m represents an average mass transfer velocity.

Inserting Equation (3.13) into (3.12) gives,

$$\dot{n}_{gw}|_{z=\delta_h} = \frac{1}{1 - \tilde{\chi}_{gs}} \left[K_m \frac{\rho_{mix}}{M_{mix}} (\tilde{\chi}_{gs} - \tilde{\chi}_{g\infty}) - \frac{\tilde{\chi}_{gs}}{1 - \tilde{\chi}_{gs}} \dot{n}_{wh} \right] . \quad (3.14)$$

Equation (3.14) is implemented as a bottom boundary condition in Paper A and B (Part II of this thesis). This is the same flux as previously used by Fer and Haugan, 2003 [38] and Haugan and Alendal, 2005 [52]. For the cases without hydrate, the water transport through the hydrate layer, \dot{n}_{wh} , naturally equals zero, and the boundary condition (Equation (3.14)) is reduced to only the first term on the right hand side.

Estimates of mass transfer velocities

In order to estimate the CO₂ flux through a hydrate layer, an estimate of the mass transfer velocity, K_m , is needed. Opdyke et al, 1987, [100] found good experimental consistency between the mass transfer from a smooth alabaster plate and the mass transfer velocity,

$$K_m = 0.078u_*Sc^{-\frac{2}{3}}, \quad (3.15)$$

where u_* represents the friction velocity, $Sc = \frac{\nu}{\kappa_{mix}}$ the Schmidt number, ν the kinematic viscosity of seawater, and κ_{mix} the molecular diffusivity of CO₂ in seawater [100]. A conservative version of Opdyke's mass transfer velocity of $K_m = 0.1u_*Sc^{-\frac{2}{3}}$ is used in the studies by Fer and Haugan, 2003 [38] and Haugan and Alendal, 2005 [52], and also in Paper A and B related to this thesis.

A new equation of state

As CO₂ is dissolved in seawater the density of the seawater increases. The density increase can be calculated as [43],

$$\rho_{mix} = \rho(S, T) + (M_{CO_2} - \alpha_{CO_2}\rho(S, T))c_T, \quad (3.16)$$

where the molar mass of CO₂ is given by $M_{CO_2} = 44.01 \cdot 10^{-3} \text{kg m}^{-3}$, the molar volume of CO₂ by $\alpha_{CO_2} = 34 \cdot 10^{-6} \text{m}^3 \text{mol}^{-1}$, and c_T is the concentration of CO₂ given in mol m^{-3} .

If the initial density is 1048kg m^{-3} , the increase in density due to dissolved CO₂ is less than 1% for saturated seawater. The Boussinesq approximation is thus still valid.

3.3.2 Solubilities of CO₂

The solubility of CO₂ in seawater is a function of temperature, pressure, and the chemical compounds in the water, and can be calculated based on the modified Henry's law [139],

$$\chi_s = K_0 f_{CO_2} \cdot \exp \left[\frac{(P_0 - P)\alpha_{CO_2}}{RT} \right]. \quad (3.17)$$

Here χ_s represents the solubility of CO₂ given in mol l^{-1} , K_0 the solubility coefficient, f_{CO_2} the fugacity, P_0 the atmospheric pressure, P the pressure, α_{CO_2} the partial molar volume of CO₂ (both given in atm), R the gas constant, and T the absolute temperature. Expressions for the solubility coefficient and the fugacity can for instance be found in Weiss, 1974 [139].

Many scientists have published values for the solubility of CO₂ in seawater, see for instance Murray and Riley, 1971 [95], Weiss, 1974 [139], and Teng et al, 1996 [128]. As saturated seawater is cooled down, some CO₂ is precipitated from the saturated seawater as CO₂ hydrate [8]. The solubility of CO₂ in seawater in the presence of hydrate is therefore lower than for the cases without hydrate [8]. Aya et al, 1997 gives solubility data for CO₂ in seawater in the company of hydrate.

In situations with relative stable pressure and temperature conditions, the solubilities in Equation (3.14) can be considered as fixed values. For deep sea cases without hydrate, solubilities based on the model by Teng et al, 1996 [128] ($\tilde{\chi}_{gs}=0.0676$) can be used, and for cases with hydrate the experimental value from Aya et al, 1997 [8] ($\tilde{\chi}_{gsh}=0.0476$) based on a pressure of 30 MPa and 3.1°C can be used.

Chapter 4

Cold-water corals

“White flowers”, referring to cold-water corals, were first mentioned in the 18th century by Erich Pontoppidan, Bishop of Bergen [115]. These “flowers” were thought to have medical effects and therefore sold to the apothecaries [115]. Lately, cold-water corals have received more attention, as we are now more aware of their importance and extension. Multitudes of organisms have their habitat affiliated with cold water corals, making their surroundings rich fishing grounds [36, 40]. The corals can be found in a wide range of sizes, from separated individuals to isolated colonies [116]. The reefs can be up to 300 m tall and have a width of several kilometers [116].

4.1 *Lophelia* Pertusa

Lophelia Pertusa is the world’s most widespread, reef-forming cold-water coral [33], and can be found all over the globe except in the polar regions [40]. Almost 1300 different species live in habitats related to *Lophelia* Pertusa [116], and the biological diversity in the vicinity of the reefs are approximately three times larger than in adjacent regions [40].

4.1.1 Anatomy

A *Lophelia* Pertusa reef can roughly be divided into three different zones [59]. At the bottom, the reef is characterized by sediments, dead skeletons, and sponges [59]. In the middle of the reef, horn corals are prevalent, and in the upper half of the reef *Lophelia* Pertusa is dominant [59].

Lophelia Pertusa builds its skeleton from calcium calcite (CaCO_3). The individual organism is an anemone coral polyp with a size of approximately 1 cm [59]. The reef consists of separate anemones merging with other anemones into

branches. Each branch grows with a velocity of approximately 6 mm per year, but due to fragmentation the total growth rate is approximately 1-2 mm per year [59]. When the branch reaches a length of approximately 5 cm it multiplies. Due to the corals ability to merge ambient branches, the coral grows strong and can sustain colonies which are up to 2 meters high [59]. At this height the colonies start to fragment. If the broken branch is located in a suitable environment, it can be the origin of a new coral colony [59].

The physiology of cold water corals can be compared with the physiology of nettles. Corals are built up of a large number of individuals (polyps), and each polyp has a simple body cave and a diffuse nerve system [59]. The corals have only one opening in their body, a mouth which is used both for eating and discharge of waste products [59]. The mouth is surrounded by tentacles.

4.1.2 Food sources

There are few observations of the food habits of cold-water corals. In previous times, scientists tried to open the coral body in order to search for leftovers of food [59]. Carl Don suggested in 1944, that the corals only ate during nighttime when it was impossible to observe them eat [59]. Today the observational methods have improved and we know that live prey is caught by the sticky tentacles of the corals [59]. *Lophelia Pertusa* mainly feed on zooplankton [116], but is also observed eating copepods and dead material [92, 115].

4.1.3 Habitats

It is a general consensus that temperature, salinity, and current velocities are important factors for settling of *Lophelia Pertusa* [59]. *Lophelia Pertusa* seems to prefer environments with temperatures ranging from 4 to 8°C [93], but is also found in waters with temperatures up to 12°C [116]. The corals prefer salinities higher than 35 psu [93]. On a global scale *Lophelia Pertusa* is observed on depths ranging from 39 to 3380 meter, and in general on firm bottom consisting of stones or solid rocks [93]. Here, the bottom is stable enough to support large reefs even under the force of strong bottom currents [115].

Though there are at present no direct experiments of the relationship between aragonite concentrations and cold-water corals, there are strong indications that the aragonite saturation horizon might be a limiting factor for the cold-water coral distribution [49]. Cold-water corals settle at much more distant depths in the Atlantic Ocean compared to in the Pacific Ocean [116]. This might be explained by the shallow aragonite saturation horizon in the Pacific Ocean [49, 116]

Food access is considered as probably the most important biological factor for settling of *Lophelia Pertusa* [59]. The corals need food in order to survive,

and there seems to be a link between high productivity in the surface layer and high concentrations of carbonate mounds [49, 143]. Since *Lophelia Pertusa* is a benthic animal located at a fixed location, the food must be transported to the coral by currents. The corals can be up to 10 000 years old, and the food access must hence have been continuous for the same amount of time. The corals are therefore assumed to settle in regions with large, constant, or periodic transport of food [115]. High current velocities give less settling of sediments in the corals and also a higher transport of nutrients. It is therefore likely that there is a correlation between abundance of coral reefs and high current velocities [116]. Still, too high current velocities might cause breakage of branches [59]. If the velocities are too high it is impossible for the polyps to catch the food in the current [59]. Based on current measurements in Trondheim it is assumed that the upper limit for beneficial current velocities are ranging between 0.5 and 1 m s⁻¹ [59].

Several theories exist to explain why corals settle in some regions and not in others, and the theory of topographically controlled settling and the hydraulic theory are some of the most well-known.

Topographic controlled distribution

There are larger occurrences of coral reefs at the shelf, shelf-break, and on topographic heights than in other parts of the ocean [88, 93]. Corals are also observed on ridges and furrows most likely generated by grounding icebergs [42]. These formations are also called iceberg plough marks. The plough marks can be traced down to 300 m depth and are mainly 5 to 8 m deep [42].

Videos made by Statoil show that there are much higher concentrations of zooplankton near the live parts of a *Lophelia* reefs than in the relative flat surrounding regions [59]. Frederiksen et al, 1992 [41] explained higher concentrations of zooplankton by observations of breaking internal tidal waves. The breaking waves increase the vertical transport, leading to a higher concentration of organic material near the bottom. Furthermore, it is observed downward transport of plankton from a layer approximately 70 m above the corals and down on the lee side of a reef [59]. Genin et al, 1986 [47] found that corals tend to settle in regions with flow acceleration.

Based on these observations, one can assume that certain topographies may be beneficial for increased food transport to cold-water corals. The topographic heights or breaks increase the encounter rate of food particles due to elevated current velocities [47]. Besides, eddies may lead to a higher concentration of food in specific regions [93]. Eddy formation will generally happen on the lee-side of the reef where there will be separation of the flow and eddies. On the upstream side, the velocities will increase. Still, this theory does not explain why coral settling is only abundant on a small fraction of all heights and clefts in the

ocean [59].

The hydraulic theory

Regions with seepage of pore water or gas are often referred to as hydraulic active areas [57]. Substances brought into the water column by such seeps are for instance, phosphate, nitrate, methane, ethane, or CO₂ [59, 60]. These tracers may affect the density and also the acidification of the ambient water masses.

Hovland et al, 1994 [58] found occurrences of *Lophelia* reefs growing in the vicinity of pockmarks at the south-western part of the Sula ridge. The concentrations of light hydrocarbon in the sediments were approximately twice the background levels. Based on these observations, Hovland and Thomsen, 1997 [61] suggested that hydrocarbon-rich sediments could lead to rich microbiological production, leading to large food access for animals feeding on bacteria [59]. *Lophelia* Pertusa is also observed on oil and gas platforms in the North Sea [46].

Later studies by Mortensen et al, 2001 [93] and Kiriakoulakis et al, 2007 [72] found no significant correlation between the density of pockmarks and the area of *Lophelia* reefs.

4.1.4 Threats

Bottom trawling in the Barents Sea started in the 1930s, and escalated in the 1960s [40]. In the early 1990s, fishermen contacted the Institute of Marine Research and claimed that corals had disappeared and their catches of fish were reduced [40]. They also expressed concern about the reefs function as nursery areas for fish [40]. Estimates indicate that between 30 and 50% of the reefs are damaged or impacted by bottom trawling [40].

For warm-water coral reefs there has been found a relationship between reduced calcification and decreased pH values [78]. This is most likely also the case for cold-water corals. In addition, hydro carbon drilling and possible leaks associated with oil and gas production may threaten the cold water corals.

4.2 Numerical studies

Thiem et al, 2006 [132] did numerical idealized simulations of the flow on the Norwegian shelf break using Bergen Ocean Model (BOM). The flow was forced with an alongslope jet and an idealized atmospheric low pressure. High encounter rates of particles were found at the shelf break, indicating that food transport is a main reason for settling at the continental margin.

As an extension of this work, Thiem et al, 2008 [131] studied encounter rates of particles for flow over an idealized coral reef, and found that the largest number of bottom hits were located at the steepest slope on the front side of the reef.

4.2.1 Assumptions

Assumptions are needed to model flow over cold-water corals using RANS models. Corals are branching and consist of numerous interconnected polyps [89]. To correctly simulate flow over corals, it is necessary to resolve the diffusive boundary layers on the branches [89]. A branch with a diameter of 1 cm and an ambient flow of 10 cm s^{-1} generates a viscous boundary layer which are approximately 0.03 cm thick [89]. The coral reefs generate rough topography. Reidenbach et al, 2006 found that the boundary layer profile above a reef looks similar to boundary layers of smoother topographies already a few tens of centimeters above the reef [111]. Existing turbulent boundary layer theory can thus be applied for flow over coral colonies.

It is found through visualization studies of warm water corals in the Red Sea, that much of the flow over a branching coral is diverted over and around the coral. As the coral geometry gets denser, a larger fraction of the flow moves outside the coral, while sparser branching and increased velocities give more water flowing through the interior of the reef [110]. Depending on the structure of the coral and the flow, the mass transfer rates through the coral branches are 50-75% of the values found outside the reef [110]. In the numerical study by Thiem et al, 2008 [131] (and also in Paper D, Part II of this thesis), it is assumed a solid reef. Hence the permeability caused by the branching corals has been neglected and replaced by a solid smooth surface. The horizontal resolution in Thiem et al, 2008 [131] ranges from 6.4 m to 0.1 m, and the branches of the corals are thereby not resolved. It thus makes sense to assume a smooth reef as a first attempt to simulate the corals. By assuming a smooth reef, turbulence generated by the small-scale topography is removed.

The branches and polyps create an increased drag. A bottom drag coefficient ranging from 0.009 to 0.015 is found through experiments with warm-water corals [111]. This is a value 4 to 6 times higher than the canonical value for the bottom drag coefficient of 0.0025 derived for muddy or sandy beds [89]. Thiem et al, 2008 [131] used a constant bottom roughness of 0.0002 m and the canonical value for the bottom drag coefficient. These values are also used in Paper D.

Thiem et al, 2008 assume that all particles that enter the lower benthic layer, are eaten by the corals and thus taken out of the simulation [131]. The food particles advect passively with the currents, and potential buoyancy effects are not included. Little is known about the eating efficiency of cold-water corals, but Yahel et al, 1998 [144] observed that planktonic food was almost completely

depleted from the water masses within a few meter of a warm-water coral reef. They also observed that the concentrations of phytoplankton and chlorophyll were reduced by 15-65% in the vicinity of coral reefs compared to in the neighbouring open waters [144].

4.2.2 A model for passive tracers

A model for passive tracers is included in Bergen Ocean Model (BOM) [20]. Pollution, passive floaters, or transport of water masses are usually either modeled as tracer concentrations or as flow of individual particles [133]. In cases where the transport is best considered as transport of individual particles, particle tracking models have benefits over concentration models [32]. Examples of such transports are settling of fish larvae or phytoplankton. Also when studying integrated properties as the residence time or release of particles from a source, it is beneficial to study particle transport by a particle tracking model [32]. When the circulation model is too coarse to represent the concentration field properly, a particle tracking model is the natural choice [32]. In a particle tracking model the computational effort is largest in the regions with the highest concentrations of particles, but in a concentration model the computational effort is the same over the entire domain [32].

In BOM the transport equation for the passive tracer, C , is given by,

$$\begin{aligned} \frac{\partial C}{\partial t} + U \frac{\partial C}{\partial x} + V \frac{\partial C}{\partial y} + W \frac{\partial C}{\partial z} \\ = \frac{\partial}{\partial x} \left(\kappa_h \frac{\partial C}{\partial x} \right) + \frac{\partial}{\partial y} \left(\kappa_h \frac{\partial C}{\partial y} \right) + \frac{\partial}{\partial z} \left(\kappa_v \frac{\partial C}{\partial z} \right) . \end{aligned} \quad (4.1)$$

Writing Equation (4.1) on flux form and introducing the sigma coordinates (Equation (2.26)) gives,

$$\begin{aligned} \frac{\partial CD}{\partial t} + \frac{\partial CUD}{\partial x} + \frac{\partial CVD}{\partial y} + \frac{\partial C\omega}{\partial \sigma} \\ = \frac{\partial}{\partial x} \left(\kappa_h D \frac{\partial C}{\partial x} \right) + \frac{\partial}{\partial y} \left(\kappa_h D \frac{\partial C}{\partial y} \right) + \frac{\partial}{\partial \sigma} \left(\frac{\kappa_v}{D} \frac{\partial C}{\partial \sigma} \right) , \end{aligned} \quad (4.2)$$

where D represents the total depth $D = H + \eta$ and ω the vertical velocity in the σ -coordinate system.

The Lagrangian position of a particle located at $\vec{X}=(X_1, X_2, X_3)$ at the time, t , can be represented by the Langevin equation [32, 133],

$$\frac{d\vec{X}}{dt} = A(\vec{X}, t) + B(\vec{X}, t)\xi(t) . \quad (4.3)$$

Here $A(\vec{X}, t)$ represents the deterministic forces, $B(\vec{X}, t)$ random forces, and $\xi(t)$ is a vector generated by random numbers. If we define,

$$\psi(t) = \int_0^t \xi(s) ds, \quad (4.4)$$

Equation (4.3) becomes equivalent to the Ito stochastic differential equation [32, 133],

$$d\vec{X} = \vec{X}(t + dt) - \vec{X}(t) = A(\vec{X}(t), t)dt + B(\vec{X}(t), t)d\psi(t). \quad (4.5)$$

Here $d\psi(t)$ is the random Wiener process fulfilling the following properties $\overline{d\psi} = 0$ and $\overline{d\psi d\psi} \propto dt$ [44]. Equation (4.4) can then be written on the discrete form,

$$\Delta\vec{X}_{n+1} = \vec{X}_{n+1} - \vec{X}_n = A(\vec{X}_n, t_n)\Delta t + B(\vec{X}_n, t_n)\sqrt{\Delta t}Z_n. \quad (4.6)$$

The parameter Z_n is a vector of independent random numbers with zero mean and unit variance [133]. If the number of particles $N \rightarrow \infty$ and the timestep $\Delta t \rightarrow 0$, Equation (4.6) is equivalent to the Fokker-Planck equation [32],

$$\frac{\partial f}{\partial t} + \frac{\partial}{\partial \vec{X}}(A f) = \nabla^2 \left(\frac{1}{2} B B^T f \right). \quad (4.7)$$

Here $f = f(\vec{X}, t | \vec{X}_0, t_0)$ represents the conditional probability density function for location of particles in the position $\vec{X}(t)$, given the initial position, \vec{X}_0 , and the initial time, t_0 [32, 133]. We want the particle tracking model to be consistent with the mass transport equation for passive tracers. To fulfill this criterion the Fokker-Planck equation must correspond to the transport equation (4.2) [133]. If Equation (4.2) is manipulated and rearranged (see Torsvik et al, 2011 [133] for a thorough description), the two equations are equivalent if the following properties are chosen,

$$A \equiv \begin{pmatrix} U + \frac{1}{D} \frac{\partial}{\partial x} (\kappa_h D) \\ V + \frac{1}{D} \frac{\partial}{\partial y} (\kappa_h D) \\ \frac{\omega}{D} + \frac{1}{D} \frac{\partial}{\partial \sigma} \left(\frac{\kappa_v}{D^2} D \right) \end{pmatrix},$$

and,

$$\frac{1}{2} B B^T \equiv \begin{pmatrix} \kappa_h & 0 & 0 \\ 0 & \kappa_h & 0 \\ 0 & 0 & \frac{\kappa_v}{D} \end{pmatrix}.$$

Hence, the particle model on discrete form may then be written as,

$$\begin{aligned}
 X_{1,(n-1)}^{(p)} - X_{1,n}^{(p)} &= \left[U_{(n)}^{(p)} + \frac{1}{D} \frac{\partial}{\partial x} (\kappa_h D) \right] \Delta t + \sqrt{2\kappa_h \Delta t} Z_n, \\
 X_{2,(n-1)}^{(p)} - X_{2,n}^{(p)} &= \left[V_{(n)}^{(p)} + \frac{1}{D} \frac{\partial}{\partial y} (\kappa_h D) \right] \Delta t + \sqrt{2\kappa_h \Delta t} Z_n, \\
 X_{3,(n-1)}^{(p)} - X_{3,n}^{(p)} &= \left[\frac{\omega_{(n)}^{(p)}}{D} + \frac{1}{D} \frac{\partial}{\partial \sigma} \left(\frac{\kappa_v D}{D^2} \right) \right] \Delta t + \sqrt{\frac{2\kappa_v}{D^2} \Delta t} Z_n.
 \end{aligned} \tag{4.8}$$

The particles are advected using either a single Euler forward time step method, or a two step Heun method (a predictor-corrector method) [133]. The particle tracking model is implemented as an independent module in BOM and is parallelized using a domain decomposition method [133].

The particle tracking method has been tested on several test cases, a closed 3D box, uniform flow over a ridge, and uniform flow over a mound. For further information about the results and the model, see Torsvik et al, 2011 [133].

Chapter 5

Summaries and further work

Topographic changes affect the flow field and thereby the transport of both passive and active tracers in the ocean. In this thesis two different kinds of tracers are studied; anthropogenic CO_2 introduced in the deep ocean and passive food particles flowing over a cold-water coral reef. As CO_2 is dissolved in seawater the density increases. CO_2 is thus an active tracer leading to a change in the equation of state. This tracer is modeled using a concentration model. The passive food particles are modeled using a particle tracking model including random walk. Both the concentration model and the particle tracking model are incorporated in a general ocean model. At present, there is a lack of data available for verification of numerical studies both concerning CO_2 storage and food access for cold water corals. It is therefore chosen to perform idealized studies to increase the number of experiments relevant for comparison.

5.1 Summary of the papers

Few laboratory experiments have been done with relevance for CO_2 behavior at 3000 m depth. In addition, the regulations related to CO_2 experiments in the ocean are strict and large scale experiments are therefore difficult and expensive to perform. Numerical models are hence an important tool to explore behavior and consequences of anthropogenic CO_2 introduced in the deep ocean. In Paper A and B the concept of a CO_2 lake located in the deep ocean is studied .

Paper A considers an idealized liquid CO_2 lake of 500 times 500 m located on a flat bottom at 3000 m depth. The study is performed in three dimensions using the z -coordinate model, the Massachusetts Institute of Technology general circulation model (MITgcm) [3]. The general circulation model is coupled with a vertical one-dimensional model, the General Ocean Turbulence Model (GOTM) [136]. GOTM includes a wide range of parametrizations for the vertical turbu-

lent mixing and has previously been coupled with the general circulation model, GETM (General Estuarine Transport Model)). The only input from the MITgcm to the GOTM is the vertical velocity shear and the buoyancy frequency. GOTM returns values for the eddy viscosities and diffusivities based on the chosen turbulence scheme. In this study, the k - ϵ model using constant stability functions is chosen to estimate the vertical eddy viscosities and diffusivities. To estimate the flux from the CO₂ lake and into the water column, a model developed by Mori and Mochizuki, 1997 [90] is used as a bottom boundary condition. The flux from the CO₂ lake depends on the friction velocity and the vertical gradient in the CO₂ concentration field above the lake. The CO₂ lake is affected by a constant velocity field of 0.05 m s⁻¹, 0.1 m s⁻¹, and 0.2 m s⁻¹. To keep the study as simple as possible, the study is done without including the effect of the Coriolis rotation and the background stratification. The CO₂ tracers is modeled by a concentration model. In less than a day, the CO₂ concentrations reaches a steady state for the near field of the lake. If the pH change is measured 250 m downstream the lake, a reduction of 2.5 pH units is observed. Such pH reductions are high enough to cause mortality for the fauna living in the vicinity of the lake [12, 13]. The dissolution rate of CO₂ from the lake and into the ambient water masses is reduced by a factor of 1.6 as the effect of hydrate is included in the CO₂ model. Papers concerning CO₂ sequestration often uses the units $\mu\text{mol s}^{-1}$ or m s^{-1} to express the dissolution rates. In Section 3.2 in Paper A, a method to convert units from $\mu\text{mol s}^{-1}$ to m s^{-1} is presented.

In Paper B, the study is extended to also include topographic effects. The paper covers three different topographies; a lake located at a flat bottom, in a valley of 10 m depth, and in a valley of 20 m depth. The simulations are done using the two-dimensional vertical slice models of the z -coordinate model, the MITgcm and the σ -coordinate model, Bergen Ocean Model (BOM) [20]. Both models are coupled with the GOTM, and the $k - \epsilon$ model is used to represent the sub-grid processes. The coupling between the MITgcm and GOTM and BOM and GOTM is validated through a Channel experiment and Couette flow. For the flat case scenarios, the coupled models give approximately the same dissolution rates from the CO₂ lake. However, as topography is included the dissolution rate decreases with the depth of the valley using the MITgcm. The opposite effect is observed using BOM. The increasing dissolution rate in the σ -coordinate model coincides with the occurrence of an eddy located in the valley and separation of the flow. The eddy causes a shift in the separation point upstream and an increase in the boundary layer thickness. The eddy enhances the vertical transport and the net transport out of the valley, leading to an increased vertical concentration gradient above the lake and a higher dissolution rate. Hence, increased turbulence activity lead to higher dissolution rates and a less suitable environment for CO₂ storage.

Paper C presents a convergence study for flow over a rounded backward-facing step. The horizontal grid sizes range from 6 to 1.5 m. The study is done to evaluate the suitability of the two models for simulating flow in a valley and over a slope, and also to check whether the eddy in Paper B is a true hydrodynamic phenomenon or due to numerical artifacts. The backward-facing step is studied using the 2D vertical (2DV) slice version of both BOM and the MITgcm. The study is done using constant eddy viscosities and diffusivities to be able to compare the results from the core of the two models with as little tuning as possible. The results are compared with laboratory experiments and numerical studies from the literature. The study includes a wide range of Reynolds numbers from the transient regime to the turbulent regime. Within the transient regime the reattachment length is longer than in the turbulent regime, in correspondence with observations by Nie and Armaly, 2004 [96]. The study shows different advantages and disadvantages of the two models, with more noise on the slope generated by the z -coordinate model compared to the σ -coordinate model. The staircase topography from the z -coordinate model gives false vertical velocities and a higher separation bubble. However, the MITgcm gives a better convergence of the reattachment point and the separation point compared to BOM. Both models show a stagnant separation point and a fluctuating reattachment point. Downstream the reattachment point downslope propagating eddies are observed. Such eddies are also observed by Bao and Dallmann, 2004 [11].

In Paper D the idealized study of flow over a backward-facing step is extended into three dimensions. The study also includes flow over a valley, a ridge, and a pockmark. All simulations are done in both 2DV and 3D using Bergen Ocean Model. This paper discusses how the inclusion of a cross-sectional dimension affects the results. Down to the separation point the flow is essentially 2DV with cross-sectional velocities 1000 times lower than the u -component. Downstream the separation point the horizontal flow is mainly downstream with span-wise eddies located in the reattachment zone and the recovering region. High vertical and cross-sectional velocities are found associated with the reattaching position in the 3D case. Furthermore, the boundary layer recovers much faster downstream the recirculating region in the 3D simulations compared to for the 2DV case. The study includes a particle tracking model developed by Torsvik et al, 2011 [133]. The passive tracers represent food particles for cold-water corals. Food particles are initiated in front of the topographic change and taken out of the simulation as they hit the bottom. The study aims to explore whether the occurrences of *Lophelia Pertusa* in for instance iceberg scours and pockmarks can be explained by pure hydrodynamic features. Previously there are found higher abundance of *Lophelia Pertusa* related to accelerated currents, breaking waves, and high surface productivity. The study reveals a correlation between eddy formation and increased encounter rates. The reattachment position is correlated to the largest

food transport to the bottom, especially for the 3D simulations with a horizontal resolution of 1.25 m. The number of particle hits at the bottom are also higher within the turbulent regime than in the transient regime.

5.2 Further work

At present, most of the knowledge related to anthropogenic CO₂ in the ocean is based on theoretical studies and laboratory experiments. In 1997, it was agreed to perform pilot studies outside Hawaii relevant for ocean sequestration of CO₂ [1]. These pilot studies were later stopped due to environmental concerns. However, field-data is needed in order to validate the models and also increase our knowledge of potential consequences of ocean sequestration, deep-sea sediment storage, and geological storage.

As the political focus has now shifted from storage in the ocean interior to storage in geological formations (and also deep-sea sediment storage), it would be interesting to study potential impact of displaced pore water due to CO₂ storage in sediments. However, such a study should preferably be combined with a field-study.

In the ocean sequestration studies in Paper A and B, there are used constant solubilities of CO₂ in seawater as input to the model by Mori and Mochizuki, 1997 [90]. To make the model valid for a wider range of temperature and pressure conditions, the constant solubilities could be replaced by a general model. Examples of such models are Duan and Sun, 2003's empirical model for solubilities of CO₂ outside the hydrate stability zone [35], and Sun and Duan, 2005's model for solubilities of CO₂ in the presence of hydrate [125]. In addition the mass transfer velocity used to estimate the CO₂ flux is based on flow over an alabaster plate. It would have been a better option to replace this mass transfer velocity by an expression based on CO₂ experiments, for instance performed in a pressure tank.

The simulations in Paper B are 2D studies. The natural next step would be to extend the study to 3D and run with a horizontal resolution corresponding to the simulations in Paper D ($\Delta x \sim 1$ m) in order to resolve the horizontal eddies in the valley. Such a study should also include dissolution of a CO₂ lake located in a pockmark. At these resolutions non-hydrostatic processes are important. Since timescales longer than the tidal cycle is considered, the Coriolis effect is important. Moreover, exposure times for phytoplankton flowing over the CO₂ lake could be estimated using the particle tracking model by Torsvik et al, 2011 [133]. Based on the exposure times and the pH profiles, the mortality rates for the benthic fauna could be estimated [7]. Ideally the extended study should be combined with a field study and involve a realistic flow field.

There is a wide dispute whether the settling conditions of cold-water corals are

related to seepage of light hydrocarbons contributing to a rich biological boundary layer or due to advected food particles. In order to evaluate the soundness of the two aforementioned hypotheses, a more realistic study should be performed. This study should consider a specific site where *Lophelia Pertusa* is known to occur, and combine numerical studies with a measurement program of both currents and the chemical compounds in the water. The numerical study should also include realistic forcing, tides, and a relevant turbulence scheme.

As cold-water corals settle, the bottom roughness increases due to growth of branches. In Paper D a constant bottom roughness parameter is used. To study how a localized increased bottom roughness would affect the flow and the particle hit rate, the bottom roughness should be increased in locations with high encounter rates. The turbulent flow near a coral is complex, and at a later point it would be desired to include a porous media model for the corals, allowing flow also through the coral branches.

Acronyms and parameters

BOM Bergen Ocean Model

Ca²⁺ Calcium ion

CaCO₃ Calcium carbonate

CCS Carbon Capture and Storage

CO₂ Carbon dioxide

CO₃²⁻ Carbonate ion

GETM General Estuarine Transport Model

GOTM General Ocean Turbulence Model

HCO₃⁺ Bicarbonate

MITgcm Massachusetts Institute of Technology general circulation model

OSPAR Oslo and Paris Commissions

Re The Reynolds number, $Re = \frac{UL}{\nu}$, [-]

Ri The Richardson number, $Ri = \frac{N^2 h^2}{U^2}$, [-]

Sc The Schmidt number, $Sc = \frac{\nu}{\kappa_{mix}}$, [-]

$A(\vec{X}, t)$ Deterministic forces in the particle tracking model (drift coefficient)

$B(\vec{X}, t)$ Random forces in the particle tracking model (diffusion coefficient)

C Concentration, [mol m⁻³]

C_D Drag coefficient, [-]

C_H Adjustable constant in the Smagorinsky parametrization, [-]

C_M Adjustable constant in the Smagorinsky parametrization, [-]

C_1 Integration constant, [-]

c_T Concentration of guest molecules in water, [mol m⁻³]

D Total depth, $D = H + \eta$, [m]

$E(k_w)$ The energy spectrum, [m³ s⁻²]

f_c The Coriolis frequency, $f = 2\Omega\sin(\theta_e)$, [s⁻¹]

f_{CO_2} The fugacity of CO₂, [atm]

G_k Production of turbulent kinetic energy due to buoyancy, [m³s⁻²]

g The constant of gravity, [m s⁻²]

h A characteristic vertical length scale, [m]

h^* Vertical position in the outer layer, [m]

K_0 Solubility coefficient, [mol l⁻¹ atm⁻¹]

K_m Mass transfer velocity, [m s⁻¹]

K_{sp}^* Solubility product, [mol² kg⁻²]

k The turbulent kinetic energy, [m²s⁻²]

k_{gw} Mass transfer coefficient, [mol m⁻² s⁻¹]

k_w The wave number, [m⁻¹]

L A characteristic length scale, [m]

l Characteristic length scale, [m]

M_g Molar mass of guest species (CO₂), [kg mol⁻¹]

M_{mix} Molar mass of water saturated with CO₂, [kg mol⁻¹]

M_w Molar mass of water, [kg mol⁻¹]

$\dot{N}_{mix_{cap}}$ Total molar flow rate through a capillary, [mol s⁻¹]

N^2 The Brunt Väisälä frequency, $N^2 = -\frac{1}{\rho} \frac{d\rho}{dz}$, [s⁻²]

n_{cap} The density of the capillaries in hydrate, [m^{-2}]
 P Reynolds averaged pressure, [$\text{kg m}^{-1}\text{s}^{-2}$]
 P_{int} Internal pressure, [$\text{kg m}^{-1}\text{s}^{-2}$]
 P_k Production of turbulent kinetic energy due to vertical shear, [m^2s^{-3}]
 P_{nh} Non-hydrostatic pressure, [$\text{kg m}^{-1}\text{s}^{-2}$]
 P_η Pressure due to the surface elevation, [$\text{kg m}^{-1}\text{s}^{-2}$]
 p Pressure, [$\text{kg m}^{-1}\text{s}^{-2}$]
 p_∞ A reference pressure outside the boundary layer, [$\text{kg m}^{-1}\text{s}^{-2}$]
 R The gas constant, [$\text{atm m}^3 \text{mol}^{-1} \text{K}^{-1}$]
 S Salinity, [psu]
 T Temperature, [K]
 t Time, [s]
 U Reynolds averaged horizontal velocity, [m s^{-1}]
 U_b The bottom velocities, [m s^{-1}]
 \bar{U}_i Reynolds averaged velocity, [m s^{-1}]
 U_∞ Free stream velocity, [m s^{-1}]
 u Horizontal velocity component, [m s^{-1}]
 \vec{u} Velocity components, u, v, w , [m s^{-1}]
 u_i The velocities, $u_i = (u, v, w)$, [m s^{-1}]
 u'_i The velocity fluctuations, [m s^{-1}]
 $\overline{u'_i u'_j}$ Reynolds stress, [m^2s^{-2}]
 $\overline{u'_i \phi'}$ The turbulent flux of the scalar ϕ
 \bar{u}_x Horizontal velocity component averaged in the x-direction, [m s^{-1}]
 u_* Friction velocity, [m s^{-1}]

V Reynolds averaged cross-sectional velocity, [m s⁻¹]
 $\dot{V}_{mix_{cap}}$ Volumetric flow through the hydrate layer of saturated water, [m³ s⁻¹]
 w Vertical velocity component, [m s⁻¹]
 \vec{X} The Lagrangian position of a particle, [m]
 x Horizontal coordinate, [m]
 y Cross-sectional coordinate, [m]
 z Vertical coordinate, [m]
 z_b Distance from the bottom to the center of the lowest grid cell, [m]
 z_0 Surface roughness, [m]
 α_{CO_2} Molar volume of CO₂, [m³ mol⁻¹]
 Δx The grid size, [m]
 δ The thickness of the boundary layer, [m]
 $\bar{\delta}$ The average thickness of the boundary layer, [m]
 δ_{i3} The Kronecker delta function, [-]
 δ_v The thickness of the viscous sublayer, [m]
 δ_{99} $u = 0.99U_\infty$ boundary layer thickness, [m]
 δ^* The displacement thickness, [m]
 ϵ The energy dissipation rate [m²s⁻³]
 ϵ_{ij3} The alternating tensor, [-]
 ϵ_p The average porosity of the hydrate layer, [-]
 $\dot{\eta}_{gh}$ Average flux of CO₂ flowing through the hydrate film, [mol m⁻² s⁻¹]
 $\dot{\eta}_{gw}|_{z=\delta}$ Average flux of CO₂ from the hydrate layer diffused into the water, [mol m⁻² s⁻¹]
 η_k The Kolmogorov scale, [m]

- $\dot{\eta}_{wg}|_{z=0}$ Average flux of water from the hydrate layer to the liquid CO₂, [mol m⁻² s⁻¹]
- $\dot{\eta}_{wh}$ Average flux of water flowing through the hydrate film, [mol m⁻² s⁻¹]
- θ The contact angle of the capillary wall on the water-side [rad]
- θ_e Latitude, [°]
- κ The Von Karman constant, $\kappa = 0.41$, [-]
- κ_k The eddy diffusivity of the turbulent kinetic energy, [m²s⁻¹]
- κ_{mix} The kinematic diffusivity of CO₂ in seawater, [m²s⁻¹]
- κ_s The diffusivity, [m²s⁻¹]
- κ_v The vertical eddy diffusivity, [m²s⁻¹]
- μ Dynamic viscosity, [kg m⁻¹s⁻¹]
- μ_{mix} The dynamic viscosity of saturated water with CO₂, [kg m⁻¹s⁻¹]
- ν Kinematic viscosity, [m²s⁻¹]
- ν_h The horizontal eddy viscosity, [m²s⁻¹]
- ν_{mix} Kinematic viscosity of CO₂, [m²s⁻¹]
- ν_v The vertical eddy viscosity, [m²s⁻¹]
- $\nu_{x_i x_j}$ The eddy viscosity, [m²s⁻¹]
- $\xi(t)$ Vector generated by random forces, [-]
- ρ Density, [kg m⁻³]
- ρ_0 A reference density, [kg m⁻³]
- σ Non-dimensional sigma coordinates, $\sigma = \frac{z-\eta}{H+\eta}$, [-]
- σ_{mix} The surface tension between water and liquid CO₂, [kg s⁻²]
- τ_0 Shear stress at the wall, [kg m⁻¹s⁻²]
- τ_b Bottom stress, [kg m⁻¹s⁻²]
- Φ Source or sink term of the scalars

ϕ Scalar properties as temperature and salinity

$\tilde{\chi}_{gs}$ Mole fraction of guest molecules (CO_2) in saturated water, [-]

$\tilde{\chi}_{gsh}$ Mole fraction of guest molecules (CO_2) in saturated water in the presence of hydrate, [-]

$\tilde{\chi}_{g\infty}$ Mole fraction of guest molecules (CO_2) further up in the water column, [-]

χ_s Saturation of guest molecules in water, [mol l^{-1}]

Ω The rotation rate of the earth, [rad s^{-1}]

Ω_{sat} Saturation rate of aragonite/calcite, [-]

ω Vertical velocity relative to the σ -coordinate system, [m s^{-1}]

Bibliography

- [1] E. Adams, M. Akai, L. Golmen, P. Haugan, H. Herzog, S. Masuda, S. Masutani, T. Ohsumi, and C. S. Wong. *An international experiment on CO₂ ocean sequestration*. Presented at the Fourth International Conference on Greenhouse Gas Control Technologies, 1998.
- [2] E. E. Adams and K. Caldeira. Ocean storage of CO₂. *Elements*, 4:319–324, 2008.
- [3] A. Adcroft, J.-M. Campin, S. Dutkiewicz, C. Evangelinos, D. Ferreira, G. Forget, B. Fox-Kemper, P. Heimbach, C. Hill, E. Hill, H. Hill, O. Jahn, M. Losch, J. Marshall, G. Maze, D. Menemenlis, and A. Molod. *MITgcm User Manual*. MIT Department of EAPS, 77 Massachusetts Ave, Cambridge, MA 02139-4307, 2008.
- [4] G. Alendal and H. Drange. Two-phase, near-field modeling of purposefully released CO₂ in the ocean. *Journal of Geophysical Research*, 106(C1):1085–1096, 2001.
- [5] L. Ametistova, J. Twidell, and J. Briden. The sequestration switch: Removing industrial CO₂ by direct ocean absorption. *The Science of the Total Environment*, 289:213–223, 2002.
- [6] D. Archer. Fate of fossil fuel CO₂ in geologic time. *Journal of Geophysical Research*, 2005.
- [7] D. I. Auerbach, J. A. Caulfield, E. E. Adams, and H. J. Herzog. Impacts of ocean CO₂ disposal on marine life: I. A toxicological assessment integrating constant-concentration laboratory assay data with variable-concentration field exposure. *Environmental Modeling and Assessment* 2, 1997.
- [8] I. Aya, K. Yamane, and H. Nairai. Solubility of CO₂ and density of CO₂ hydrate at 30 MPa. *Energy*, 22(2/3):263–271, 1997.

- [9] I. Aya, K. Yamane, and N. Yamada. Simulation experiment of CO₂ storage in the basin of deep-ocean. *Energy Conversion and Management*, 36(6-9):485-488, 1995.
- [10] S. Bachu. *Geological perspectives of global climate change*, chapter Geological sequestration of CO₂: Is leakage unavoidable and acceptable?, pages 285–304. AAPG Studies in Geology 47. American Association of Petroleum Geologists, 2001.
- [11] F. Bao and U. C. Dallmann. Some physical aspects of separation bubble on a rounded backward-facing step. *Aerospace Science and Technology*, 8:83–91, 2004.
- [12] J. P. Barry, K. R. Buck, C. Lovera, L. Kuhnz, and P. J. Whaling. Utility of deep sea CO₂ release experiments in understanding the biology of a high-CO₂ ocean: Effects of hypercapnia on deep sea meiofauna. *Journal of Geophysical Research*, 110(C09S12), 2005.
- [13] J. P. Barry, K. R. Buck, C. F. Lovera, L. Kuhnz, P. J. Whaling, E. T. Peltzer, P. Walz, and P. G. Brewer. Effects of direct ocean CO₂ injection on deep-sea meiofauna. *Journal of Oceanography*, 60:759–766, 2004.
- [14] G. K. Batchelor. *An introduction to fluid dynamics*. Cambridge University Press, 1998.
- [15] N. R. Bates and A. J. Peters. The contribution of atmospheric acid deposition to ocean acidification in the subtropical North Atlantic Ocean. *Marine Chemistry*, 107:547–558, 2007.
- [16] H. Z. Baumert, J. H. Simpson, and J. Sundermann. *Marine turbulence*. Cambridge University Press, Cambridge, UK, 2005. ISBN: 0-521-83789-8.
- [17] J. Beardall and J. A. Raven. The potential effects of global climate change on microalgal photosynthesis, growth and ecology. *Phycologia*, 43(1):26–40, 2004.
- [18] S. M. Benson and D. R. Cole. CO₂ sequestration in deep sedimentary formations. *Elements*, 4:325–311, 2008.
- [19] J. Berntsen. Internal pressure errors in sigma-coordinate ocean models. *Journal of Atmospheric and Oceanic Technology*, 19:1403–1414, 2002.

- [20] J. Berntsen. USERS GUIDE for a modesplit σ -coordinate numerical ocean model. Technical Report 4.1, University of Bergen, Johs. Bruns gt. 12, N-5008 BERGEN, 2004.
- [21] J. Berntsen. A perfectly balanced method for estimating the internal pressure gradients in σ -coordinate ocean models. *Ocean Dynamics*, 2011.
- [22] R. B. Bird, W. E. Stewart, and E. N. Lightfoot. *Transport phenomena*. John Wiley & Sons, Inc, 2002. ISBN: 0-471-41077-2.
- [23] V. Bjerknes. Das Problem der Wettervorhersage, betrachtet vom Standpunkte der Mechanik und der Physik. *Meteorologische Zeitschrift*, 21:1–7, 1904. (The problem of weather prediction, considered from the viewpoints of mechanics and physics, translated and edited by Volken E. and S. Brönnimann. – *Meteorologische Zeitschrift* 18 (2009), 663–667).
- [24] A. F. Blumberg and G. L. Mellor. *Three-dimensional coastal ocean models, 1-16*, chapter A description of a three-dimensional coastal ocean circulation model. American Geophysical Union, 1987.
- [25] P. G. Brewer, G. Friederich, E. T. Peltzer, and Jr. F. M. Orr. Direct experiments on the ocean disposal of fossil fuel CO₂. *Science*, 284:943–945, 1999.
- [26] P. G. Brewer, E. Peltzer, I. Aya, P. Haugan, R. Bellerby, K. Yamane, R. Kojima, P. Walz, and Y. Nakajima. Small scale field study of an ocean CO₂ plume. *Journal of Oceanography*, 60:751–758, 2004.
- [27] E. Brown, A. Colling, D. Park, J. Phillips, D. Rothery, and J. Wright. *Sea-water: Its composition properties and behavior*, volume 2 of 330. The Open University, 1989. ISBN: 0-7506-3715-3.
- [28] K. Bryan. A numerical method for the study of the circulation of the world ocean. *Journal of Computational Physics*, 4(3):347–376, 1969.
- [29] H. Burchard. *Applied turbulence modeling in marine waters*. Springer, Berlin, Heidelberg, New York, 2002. ISBN: 3-540-43795-9.
- [30] K. Caldeira and M. E. Wickett. Anthropogenic carbon and ocean pH. *Nature*, 425(6956):365, 2003.
- [31] M. A. Celia and S. Bachu. Geological sequestration of CO₂: Is leakage unavoidable and acceptable? *Proceedings of the Sixth International Greenhouse Gas Technologies Conference, Kyoto, Japan*, Vol 1:477–482, 2003. Edited by Y. Kaya and J. Gale, Pergamon, New York.

- [32] K. N. Dimou and E. E. Adams. A random-walk, particle tracking model for well-mixed estuaries and coastal waters. *Estuarine, Coastal and Shelf Science*, 37:99–110, 1993.
- [33] L. A. Dodds, J. M. Roberts, A. C. Taylor, and F. Marubinic. Metabolic tolerance of the cold-water coral *Lophelia Pertusa* (scleractinia) to temperature and dissolved oxygen change. *Journal of Experimental Marine Biology and Ecology*, 349(Issue 2):205–214, 2007.
- [34] S. C. Doney, V. J. Fabry, R. A. Feely, and J. A. Kleypas. Ocean acidification: The other CO₂ problem. *Annual Review of Marine Science*, pages 169–192, 2008. doi: 10.1146/annurev.marine.010908.163834.
- [35] Z. Duan and R. Sun. An improved model calculating CO₂ solubility in pure water and aqueous NaCl solutions from 273 to 533 K and from 0 to 2000 bar. *Chemical Geology*, 193:257–271, 2003.
- [36] G. C. A. Duineveld, M. S. S Laveleye, and E. M. Berghuis. Particle flux and food supply to a seamount cold-water coral community (Galicia Bank, NW Spain). *Marine Ecology Progress Series*, 277:13–23, 2004.
- [37] R. A. Feely, C. L. Sabine, K. Lee, W. Berelson, J. Kleypas, V. J. Fabry, and F. J. Millero. Impact of anthropogenic CO₂ on the CaCO₃ system in the oceans. *Science*, 305:362–366, 2004.
- [38] I. Fer and P. M. Haugan. Dissolution from a liquid CO₂ lake disposed in the deep ocean. *Limnology and Oceanography*, 48(2):872–883, 2003.
- [39] J. H. Ferziger and M. Perić. *Computational methods for fluid dynamics*. Springer, 3rd edition, 2002. ISBN: 3-540-42074-6.
- [40] J. H. Fosså, P. B. Mortensen, and D. M. Furevik. The deep-water coral *Lophelia Pertusa* in Norwegian waters: Distribution and fishery impacts. *Hydrobiologia*, 471:1–12, 2002.
- [41] R. Frederiksen, A. Jensen, and H. Westerberg. The distribution of the scleractinian coral *Lophelia Pertusa* around the Faroe Islands and the relation to internal tidal mixing. *SARSIA*, 1992.
- [42] A. Freiwald, J. B. Wilson, and R. Henrich. Grounding pleistocene icebergs shape recent deep-water coral reefs. *Sedimentary Geology*, 125:1–8, 1999.
- [43] J. E. Garcia. Density of aqueous solutions of CO₂. *Report LBNL-49023 Lawrence Berkeley National Laboratory*, 2001. 8p.

- [44] C. W. Gardiner. *Handbook of stochastic methods for physics, chemistry and the natural sciences*. Springer Series in Synergetics. Springer-Verlag, 2nd edition, 1985. ISBN: 0-387-11357-6.
- [45] J. M. Gary. Estimation of truncation errors in transformed coordinate, primitive equation atmospheric models. *Journal of Atmospheric Science*, 30:223–233, 1973.
- [46] S. E. Gass and J. M. Roberts. The occurrence of the cold-water coral *Lophelia Pertusa* (scleractinia) on oil and gas platforms in the North Sea: Colony growth, recruitment and environmental controls on distribution. *Marine Pollution Bulletin*, 52:549–559, 2006.
- [47] A. Genin, P. K. Dayton, P. F. Lonsdale, and F. N. Spiess. Corals on seamount peaks provide evidence of current acceleration over deep-sea topography. *Letters to Nature*, 322:59–61, 1986.
- [48] M. C. Gregg. Diapycnal mixing in the thermocline: A review. *Journal of Geophysical Research*, 92(C5):5249–5286, 1987.
- [49] J. M. Guinotte, J. Orr, S. Cairns, A. Freiwald, L. Morgan, and R. George. Will human-induced changes in seawater chemistry alter the distribution of deep-sea scleractinian corals. *Frontiers in Ecology and the Environment*, 4:141–146, 2006.
- [50] D. B. Haidvogel and A. Beckmann. *Numerical ocean circulation modeling*, volume 2 of *Series on Environmental Science and Management*. Imperial College Press, 1998.
- [51] E. Hanert, D. Deleersnijder, S. Blaise, and J.-F. Remacle. Capturing the bottom boundary layer in finite element ocean models. *Ocean Modeling*, 17:153–162, 2007.
- [52] P. M. Haugan and G. Alendal. Turbulent diffusion and transport from a CO₂ lake in the deep ocean. *Journal of Geophysical Research*, 110:C09S14, 2005.
- [53] P. M. Haugan and H. Drange. Effects of CO₂ on the ocean environment. *Energy Conversion and Management*, 37(6-8):1019–1022, 1996.
- [54] K. C. Hester, E. T. Peltzer, W. J. Kirkwood, and P. G. Brewer. Unanticipated consequences of ocean acidification: A noisier ocean at lower pH. *Geophysical Research Letter*, 2008.

- [55] O. Hoegh-Guldberg. Coral reefs under rapid climate change and ocean acidification. *Science*, 318:1737–1742, 2007. doi: 10.1126/science.1152509.
- [56] K. Z. House, D. P. Schrag, C. F. Harvey, and K. S. Lackner. Permanent carbon dioxide storage in deep-sea sediments. *PNAS*, 103(33):12291–12295, 2006.
- [57] M. Hovland. *Cold-water corals and ecosystems*, chapter Pockmark-associated coral reefs at the Kristin field off Mid-Norway, pages 623–632. Springer-Verlag, 2005.
- [58] M. Hovland, R. Farestveit, and P. B. Mortensen. Large cold-water coral reefs off mid-Norway - a problem for pipe-laying? *Conference Proceedings (3), Oceanology International*, pages 8–11, 1994.
- [59] M. Hovland and P. B. Mortensen. *Norske korallrev og prosesser i havbunnen*. John Grieg Forlag, 1999.
- [60] M. Hovland, P. B. Mortensen, T. Brattegard, P. Stras, and K. Rokoengen. Ahermatypic coral banks of Mid-Norway: Evidence for a link with seepage of light hydrocarbons. *PALOIS*, 13(2):189–200, 1998.
- [61] M. Hovland and E. Thomsen. Cold-water corals - are they hydrocarbon seep related? *Marine Geology*, 137:159–164, 1997.
- [62] T. Ilyina, R. E. Zeebel, and P. G. Brewer. Future ocean increasingly transparent to low-frequency sound owing to carbon dioxide emissions. *Nature Geoscience*, 3:18 – 22, 2010.
- [63] R. L. Ingermann, M. L. Robinson, and J. G. Cloud. Respiration of steelhead trout sperm: Sensitivity to pH and carbon dioxide. *Journal of Fish Biology*, 62(1):13–23, 2003.
- [64] IPCC. *Special report on carbon dioxide capture and storage*. Prepared by Working Group III of the Intergovernmental Panel on Climate Change. [B. Metz, O. Davidson, H. C. de Coninck, M. Loos and L. A. Meyer (Eds.)]. Cambridge University Press, Cambridge, United Kingdom and New York, NY, USA, December 2005. <http://www.ipcc.ch/activity/srccs/index.htm>.
- [65] A. Ishimatsu, T. Kikkawa, M. Hayashi, K.-S. Lee, and J. Kita. Effects of CO₂ on marine fish: Larvae and adults. *Journal of Oceanography*, 60:731–741, 2004.

- [66] S. R. Jayne, L. C. St Laurent, and S. T. Gille. Connections between ocean bottom topography and earth's climate. *Oceanography*, 17(1):65–74, 2004.
- [67] J. Jiménez. Turbulent flows over rough walls. *Annual Review of Fluid Mechanics*, 36:176–196, 2004.
- [68] Y. Kano, T. Sato, J. Kita, S. Hirabayashi, and S. Tabeta. Model prediction on the rise of pCO₂ in uniform flows by leakage of CO₂ purposefully stored under the seabed. *International Journal of Greenhouse Gas Control*, 3:617–625, 2009.
- [69] L. H. Kantha and C. A. Clayson. *Numerical models of oceans and oceanic processes*, volume 66 of *International Geophysics Series*. Academic Press, 2000. ISBN 0-12-434068-7.
- [70] L. H. Kantha and C. A. Clayson. *Small scale processes in geophysical fluid flows*, volume 67 of *International Geophysics Series*. Academic Press, 2000. ISBN 0-12-434070-9.
- [71] D. E. Kelley and K. A. Van Scoy. A basinwide estimate of vertical mixing in the upper pycnocline: Spreading of bomb tritium in the North Pacific Ocean. *Journal of Physical Oceanography*, 1999.
- [72] K. Kiriakoulakis, A. Freiwald, and E. Fisher. Organic matter quality and supply to deep-water coral/mound systems of the NW European Continental Margin. *International Journal of Earth Science*, 96:159–170, 2007.
- [73] H. Koide, M. Takahashi, Y. Shindo, Y. Tazaki, M. Iijima, K. Ito, N. Kimura, and K. Omata. Hydrate formation in sediments in the sub-seabed disposal of CO₂. *Energy*, 1997.
- [74] A. N. Kolmogorov. The local structure of turbulence in incompressible viscous fluid for very large Reynolds numbers. *Dokl. Akad. Nauk SSSR*, 1941. Reprinted in: Proceedings: Mathematical and Physical Sciences (434), 1890 pp 9-13, 1991.
- [75] P. K. Kundu and I. M. Cohen. *Fluid mechanics*. Elsevier Academic Press, 3rd edition, 2004. ISBN: 0-12-178253-0.
- [76] H. Kurihara, S. Shimode, and Y. Shirayama. Effects of raised CO₂ concentration on the egg production rate and early development of two marine copepods (*Acartia steueri* and *Acartia erythraea*). *Marine Pollution Bulletin*, 49:721–727, 2004.

- [77] H. Kurihara, S. Shimode, and Y. Shirayama. Sub-lethal effects on elevated concentration of CO₂ on planktonic copepods and sea urchins. *Journal of Oceanography*, 60:743–750, 2004.
- [78] C. Langdon, T. Takahashi, C. Sweeney, D. Chipman, J. Goddard, F. Marubini, H. Aceves, H. Barnett, and M. J. Atkinson. Effect of calcium carbonate saturation state on the calcification rate of an experimental coral reef. *Global Biogeochemical Cycles*, 14(2):639–654, 2000.
- [79] J. R. Ledwell, E. T. Montgomery, K. L. Poltzin, L. C. St Laurent, R. W. Schmitt, and J. M. Toole. Evidence for enhanced mixing over rough topography in the abyssal ocean. *Nature*, 403:179–182, 2000.
- [80] J. R. Ledwell, A. J. Watson, and C. S. Schmitt. Mixing of a tracer in the pycnocline. *Journal of Geophysical Research*, 103(C10):21499–21529, 1998.
- [81] London Convention. Risk assessment and management framework for CO₂ sequestration in sub-seabed geological structures (CS-SSGS), 2007.
- [82] E. N. Lorenz. Deterministic nonperiodic flow. *Journal of the Atmospheric Sciences*, 20:130–141, 1963.
- [83] C. Marchetti. On geoengineering and the CO₂ problem. *Climate Change*, 1:59–68, 1977.
- [84] J. Marshall, C. Hill, L. Perelman, and A. Adcroft. Hydrostatic, quasi-hydrostatic, and nonhydrostatic ocean modeling. *Journal of Geophysical Research*, 102(C3):5733–5752, 1997.
- [85] R. May. *It must be beautiful. Great equations of modern science*, chapter The best possible time to be alive: The logistic map, pages 28–45. Granta Books, 2003.
- [86] J. D. McCalpin. A comparison of second-order and fourth-order pressure gradient algorithms in a σ -coordinate ocean model. *International Journal of Numerical Methods in Fluids*, 18:361–383, 1994.
- [87] G. L. Mellor, L.-Y. Oey, and T. Ezer. Sigma coordinate pressure gradient errors and the seamount problem. *Journal of Atmospheric and Oceanic Technology*, 15:1122–1131, 1998.
- [88] C. Messing, A. C. Neumann, and J. C. Lang. Biozonation of deep-water lithoherms and associated hardgrounds in the northeastern straits of

- Florida. *Research reports, Society for Sedimentary Geology, Palaios*, 5:15–33, 1990.
- [89] S. G. Monismith. Hydrodynamics of coral reefs. *Annual Review of Fluid Mechanics*, 39:37–55, 2007.
- [90] Y. Mori and T. Mochizuki. Mass transport across clathrate hydrate films - a capillary permeation model. *Chemical Engineering Science*, 52(20):3613–3616, 1997.
- [91] Y. H. Mori. Clathrate hydrate formation at the interface between liquid CO₂ and water phases - a review of rival models characterizing "hydrate films". *Energy Conversion Management*, 38(15):1537–1557, 1998.
- [92] P. B. Mortensen. Aquarium observations on the deep-water coral *Lophelia Pertusa* (l. 1758) (scleractinia) and selected associated invertebrates. *Opheelia*, 54:83–104, 2001.
- [93] P. B. Mortensen, M. T. Hovland, J. H. Fosså, and D. M. Furevik. Distribution, abundance and size of *Lophelia Pertusa* coral reefs in mid-Norway in relation to seabed characteristics. *Journal of the Marine Biological Association of the United Kingdom*, 81:581–597, 2001.
- [94] W. Munk. Abyssal recipes. *Deep-Sea Research*, 13:707–733, 1966.
- [95] C. N. Murray and J. P. Riley. The solubility of gases in distilled water and seawater - IV. Carbon dioxide. *Deep-sea Research*, 18:533–541, 1971.
- [96] J. H. Nie and B. F. Armaly. Reverse flow regions in three-dimensional backward-facing step flow. *International Journal of Heat and Mass Transfer*, 47:4713–4720, 2004.
- [97] S. Nilsson and W. Shopfhauser. The carbon-sequestration potential of a global afforestation program. *Climatic Change*, 30:267–293, 1995.
- [98] J. M. Nordbotten, M. A. Celia, S. Bachu, and H. Dahle. Semianalytical solution for CO₂ leakage through an abandoned well. *Environmental Science Technology*, 39:602–611, 2005.
- [99] E. H. Oelkers and D. R. Cole. Carbon dioxide sequestration a solution to a global problem. *Elements*, 4:305–310, 2008.
- [100] B. N. Opdyke, G. Gust, and J. R. Ledwell. Mass transfer from smooth alabaster surfaces in turbulent flows. *Geophysical Research Letters*, 14(11):1131–1134, 1987.

- [101] W. G. Ormerod, P. Freund, and A. Smith. Ocean storage. Technical report, I. E. A. Greenhouse Gas R&D Programme, 2002. 2nd Edition. ISBN: 1-898373-30-2.
- [102] J. C. Orr. Modeling of ocean storage of CO₂ - the GOSAC study. *International Energy Agency, Greenhouse Gas R&D Programme*, Report PH4/37:96 p, 2004.
- [103] J. C. Orr, V. J. Fabry, O. Aumont, L. Bopp, S. C. Doney, and R. A. Feely et al. Anthropogenic ocean acidification over the twenty-first century and its impact on calcifying organisms. *Nature*, 437(29):681–686, 2005.
- [104] OSPAR Convention. OSPAR decision 2007/1 to prohibit the storage of carbon dioxide streams in the water column or on the sea-bed. Annex 5.
- [105] OSPAR Convention. OSPAR guidelines for risk assessment and management of storage of CO₂ streams in geological formations, 2007. Annex 7.
- [106] S. Pacala and R. Socolow. Stabilization wedges: Solving the climate problem for the next 50 years with current technologies. *Science*, 305:968–972, 2004.
- [107] The European Parliament and the Council. Directive 2009/31/EC of the European Parliament and of the council of 23 april 2009 on the geological storage of carbon dioxide and amending council directive 85/337/EEC, European Parliament and council directives 2000/60/EC, 2001/80/EC, 2004/35/EC, 2006/12/EC, 2008/1/EC and regulation (EC) no 1013/2006. *Official Journal of the European Union*, 2009.
- [108] K. L. Poltzin, J. M. Toole, J. R. Ledwell, and R. W. Schmitt. Spatial variability of turbulent mixing in the abyssal ocean. *Science*, 276:93–96, 1997.
- [109] J. Raven. Ocean acidification due to increasing atmospheric carbon dioxide. The Royal Society, 2005. Policy document 12/05, ISBN 0 85403 617 2.
- [110] M. A. Reidenbach, J. R. Koseff, S. G. Monismith, J. V. Steinbuck, and A. Genin. The effects of waves and morphology on mass transfer within branched reef corals. *Limnology and Oceanography*, 51(2):1134–1141, 2006.
- [111] M. A. Reidenbach, S. G. Monismith, J. R. Koseff, G. Yahel, and A. Genin. Boundary layer turbulence and flow structure over a fringing coral reef. *Limnology and Oceanography*, 51(5):1956–1968, 2006.

- [112] O. Reynolds. An experimental investigation of the circumstances which determine whether the motion of water shall be direct or sinuous, and the law of resistance in parallel channels. *Philosophical Transactions of the Royal Society of London*, 174:935–982, 1883.
- [113] O. Reynolds. On the dynamical theory of incompressible viscous fluids and the determination of the criterion. *Philosophical Transactions of the Royal Society of London. A.*, 186:123–164, 1895.
- [114] O. Reynolds. *Papers on Mechanical and Physical subjects*, volume 2, chapter 48. On the two manners of motion of water, pages 153–162. Cambridge: Cambridge Univ. Press, 1901.
- [115] J. M. Roberts, A. Wheeler, A. Freiwald, and S. Cairns. *Cold-water corals, The biology and geology of deep-sea coral habitats*. Cambridge University Press, 2009. ISBN: 978-0-521-88485-3.
- [116] J. M. Roberts, A. J. Wheeler, and A. Freiwald. Reefs of the deep: The biology and geology of cold-water coral ecosystems. *Science*, 2006.
- [117] B. Rost and U. Riebesell. *Coccolithophores: From molecular processes to global impact*, chapter Coccolithophores and the biological pump: Responses to environmental changes, pages 99–125. Springer, 2004.
- [118] J. M. Santana-Casiano, M. González-Dávila, M. J. Rueda, O. Llinás, and S.-F. González-Dávila. The interannual variability of oceanic CO₂ parameters in the northeast Atlantic subtropical gyre at the ESTOC site. *Global Biogeochemical Cycle*, 21(GB1015), 2007.
- [119] D. A. Segar. *Introduction to ocean sciences*. Wadsworth Publishing Company, 1998. ISBN: 0-314-09705-8.
- [120] A. J. Semtner. Modeling ocean circulation. *Science*, 8:1379–1385, 1995. doi:10.1126/science.269.5229.1379.
- [121] U. Siegenthaler and J. L. Sarmiento. Atmospheric carbon dioxide and the ocean. *Nature*, 365:119–125, 1993.
- [122] M. S. Silberberg. *Chemistry, The molecular nature of matter and change*. McGraw Hill, 2nd edition edition, 2000. ISBN: 0-697-39597-9.
- [123] J. Smagorinsky. General circulation experiments with the primitive equations. 1. The basic experiment. *Monthly Weather Review*, 91(3):99–164, 1963.

- [124] G. S. Stelling and J. A. T. M. van Kester. On the approximation of horizontal gradients in sigma coordinates for bathymetry with steep bottom slopes. *International Journal of Numerical Methods in Fluids*, 18:915–935, 1994.
- [125] R. Sun and Z. Duan. Prediction of CH₄ and CO₂ hydrate phase equilibrium and cage occupancy from ab initio intermolecular potentials. *Geochimica et Cosmochimica Acta*, 69(18):4411–4424, 2005.
- [126] J. C. Sylvan. How to protect a coral reef: The public trust doctrine and the law of the sea. *Sustainable Development Law & Policy*, pages 32–35, 2006.
- [127] M. N. Tamburri, E. T. Peltzer, G. E. Friederich, I. Aya, K. Yamane, and P. G. Brewer. A field study of the effects of CO₂ ocean disposal on mobile deep-sea animals. *Marine Chemistry*, 72:95–101, 2000.
- [128] H. Teng, S. M. Masutani, C. M. Kinoshita, and G. C. Nihous. Solubility of CO₂ in the ocean and its effect on CO₂ dissolution. *Energy Conversion and Management*, 37(6-8):1029–1038, 1996.
- [129] H. Tennekes. The logarithmic wind profile. *Journal of Atmospheric Sciences*, 30:234–238, 1973.
- [130] Ø. Thiem and J. Berntsen. Internal pressure errors in sigma-coordinate ocean models due to anisotropy. *Ocean Modelling*, 12:140–156, 2006.
- [131] Ø. Thiem, J. Berntsen, K. Selvikvåg, and J. H. Fosså. Numerical study of particle encounters with an idealized coral reef with focus on grid resolutions and viscosities. *BCCS Technical Report Series*, 24, 2008. <http://www.bccs.uni.no/publications/files/techrep24.pdf>.
- [132] Ø. Thiem, E. Ravagnan, J. H. Fosså, and J. Berntsen. Food supply mechanisms for cold-water corals along a continental shelf edge. *Journal of Marine Systems*, 60:207–219, 2006.
- [133] T. Torsvik, H. Avlesen, and Ø. Thiem. Tracking of passive, neutrally buoyant particles using the Bergen Ocean Model. Technical report, BCCS Technical Report Series, nr. 27, 2011. <http://www.bccs.uni.no/publications/files/techrep27.pdf>.
- [134] C. Tsouris, P. Brewer, E. Peltzer, P. Walz, D. Riestenberg, L. Liang, and O. R. West. Hydrate composite particles for ocean carbon sequestration: Field verification. *Environmental Science & Technology*, 38:2470–2475, 2004.

- [135] C. Turley. Impacts of changing ocean chemistry in a high-CO₂ world. *Mineralogical Magazine*, 72(1):359–362, 2008.
- [136] L. Umlauf, H. Burchard, and K. Bolding. GOTM source code and test case documentation. Version 4.0.
- [137] E. W. Vetter and C. R. Smith. Insights into the ecological effects of deep ocean CO₂ enrichment: The impacts of natural CO₂ venting at Loihi seamount on deep sea scavengers. *Journal of Geophysical Research*, 110(C09S13), 2005. doi: 10.1029/2004JC002617.
- [138] G. L. Weatherly and P. J. Martin. On the structure and dynamics of the oceanic bottom boundary layer. *Journal of Physical Oceanography*, 8:557–570, 1978.
- [139] R. F. Weiss. Carbon dioxide in water and seawater: The solubility of a non-ideal gas. *Marine Chemistry*, 2:203–215, 1974.
- [140] P. K. Weyl. *Oceanography An introduction to the marine environment*. John Wiley & Sons, Inc, 1970. ISBN: 471-93744-4.
- [141] F. M. White. *Fluid mechanics*. McGraw Hill, 5th edition, 2005. ISBN: 0-07-240217-2.
- [142] F. M. White. *Viscous fluid flow*. McGraw Hill, 3rd edition, 2006. ISBN: 978-0-07-240231-5.
- [143] M. White, C. Mohn, H. de Stigter, and G. Mottram. *Cold-water corals and ecosystems*, chapter Deep-water coral development as a function of hydrodynamics and surface productivity around the submarine banks of the Rockall Trough, NE Atlantic, pages 503–514. Springer-Verlag Berlin Heidelberg, 2005.
- [144] G. Yahel, A. F. Post, K. Fabricius, D. Marie, D. Vaultot, and A. Genin. Phytoplankton distribution and grazing near coral reefs. *Limnology and Oceanography*, 4:551–563, 1998.